MASTERARBEIT | MASTER'S THESIS

Titel | Title

(Bio-)Sensor development for Vascular Endothelial Growth factor monitoring

verfasst von | submitted by

Viktoria Mayer BSc

angestrebter akademischer Grad | in partial fulfilment of the requirements for the degree of

Master of Science (MSc)

Wien | Vienna, 2024

Studienkennzahl lt. Studienblatt | Degree programme code as it appears on the student record sheet:	UA 066 862
Studienrichtung lt. Studienblatt | Degree programme as it appears on the student record sheet:	Masterstudium Chemie
Betreut von | Supervisor:	Univ.-Prof. Mag. Dr. Peter Lieberzeit

ACKNOWLEDGEMENTS

The research activities for this thesis were carried out through a collaborative effort involving the Lieberzeit Group at the University of Vienna and the Centre of Electrochemistry and Surface Technology GmbH (CEST) in Tulln. Both I like to thank for making this thesis possible.

The main experiments were conducted in Tulln, where I had been supervised by Dr. Philipp Fruhmann, Dr. Jakub Dostálek and Katharina Schmidt. I'm glad they were constantly helping and supporting me throughout my work. Moreover, I want to thank the whole research group for their welcoming and supportive attitude.

Many thanks go to Prof. Dr. Peter Lieberzeit for accepting me as a master's student and especially to Julia Völkle, who was helping me with all the experiments in the department of physical chemistry in the University of Vienna.

My deepest gratitude go to all my friends from university who always helped me with any difficulties as well as to my boyfriend who supported from the very beginning to achieve this goal.

TABLE OF CONTENTS

List of abbreviations

cAb capture antibody

dAb detection antibody

ELISA enzyme-linked immunosorbent assay

HCl Hydrochloride

$MgCl_2$ Magnesium chloride

MIPs Molecularly imprinted polymers

NaOH Sodium hydroxide

NRP-1 Neuropilin-1

PBST Phosphate-buffered saline with Tween

PDI Polydispersity Index

PEG-Biotin Polyethylenglycol-Biotin

PEG-OH Polyethylenglycol-OH

QCM Quartz crystal microbalance

SAM Self-assembled monolayer

SPR Surface Plasmon resonance

VEGF Vascular endothelial growth factor

VEGFR-1 Vascular endothelial growth factor receptor 1

VEGFR-2 Vascular endothelial growth factor receptor 2

1. Introduction and aim of the thesis

The vascular development in an organism comprises two main processes: *vasculogenesis*, which involves the formation of blood vessels from endothelial cells derived from precursor cells such as hemangioblasts and angioblasts. This process results in the formation of a primitive, poorly differentiated primary vascular plexus. The second process, *angiogenesis*, involves the growth, sprouting, and remodeling of this initial tubular network to establish a mature vascular system.[1,2] This system provides its surrounding environment the continuous supply with nutrients and oxygen as well as the ability for the transportation of hormones to coordinate physiologic responses and to enable cell-cell communication. Its formation is mediated by the so called Vascular endothelial growth factor (VEGF), which was discovered in the 1980s by three independent research groups.

Further characterization experiments have demonstrated that it is potentially angiogenic and mitogen specific, when interacting with endothelial cells; it promotes their growth, migration, and survival as well as it regulates blood vessel permeability and vasodilation.[3] Ferrara *et al.* showed the necessity of VEGF as a central regulator of *vasculogenesis*, by using a technique of targeted gene disruption in mice. They revealed that only precise VEGF concentration gradients lead to a normal development of the embryo whereas aberrations directly lead to an abnormal angiogenic behavior.[4]

Although this remarkable system is designed to supply the organism, tumors exploit it by taking advantage of the *angiogenesis* to satisfy their own nutritional requirements and to create a pathway for metastasizing to other tissues by destabilizing the walls of mature blood vessels. Figure 1 shows the formation of the vascular system and the subsequent sprouting of *angiogenesis*.

However, the reason why research started to focus on the investigation of VEGF and its role in facilitating or inhibiting *angiogenesis* derived from the fact that it has been associated with several pathologies such as atherosclerosis[5], diabetic retinopathy[6,7], amyotrophic lateral sclerosis (ALS)[8], arthritis, cardiovascular disease and most prominently malignant cell growth *i.e.* tumor growth.[9,10]

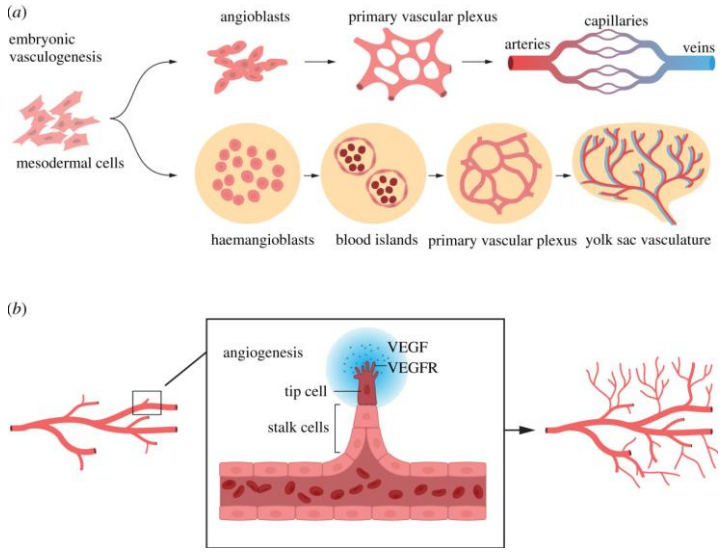

Figure 1:(a) The vascular system originates from mesodermal cells. Those differentiate in angioblasts and hemangioblasts and form a primary vascular plexus. In the case of embryonic vasculogenesis, the blood vessels within the vascular plexus develop arterial (red) and venous (blue) characteristics along an arterial-capillary-venous axis. In comparison during extraembryonic vasculogenesis the yolk sac vasculature is built. (b) In the process of angiogenesis, new blood vessels form through sprouting from an existing vascular network. This sprouting is initiated by a leading tip cell in response to vascular endothelial growth factor (VEGF) and its receptors, VEGFR. Following the tip cell, stalk cells develop to form the lumen of the newly sprouting vessel. [11]

Thus, VEGF within the blood stream can yield information on health status of an individual, *i.e.* it acts as a biomarker. For that reason, this thesis focused on developing a sensor to detect VEGF via two approaches.

The first approach aimed at analyzing VEGF directly via Surface Plasmon Resonance (SPR) by sandwiching the analyte via an Enzyme Linked Immunosorbent Assay. The second approach relied on direct detection of a particular VEGF epitope sequence and its complementary MIPs via QCM. The MIPs were synthesized to match the epitope sequence.

A first goal for the first approach included finding a matching capture antibody - antigen-pair. Moreover, it was necessary to optimize the detection antibody concentration, in order to avoid too high signals from unspecific binding. The next step was to establish a titration curve to figure out the concentrations of VEGF in unknown samples. The steps comprised of finding a suitable regeneration solution, followed by control experiments regarding the selectivity of the system as well as the influence of other serum components on the system.

The goal for the second approach was to establish a system to detect a VEGF epitope via tailormade nanoMIPs. These MIPs were used on a QCM and have the potential to be also implemented in SPR-based sensing in the future. For that reason, two different mixtures of MIPs were synthesized. As a starting point the VEGF epitope template was immobilized on a solid phase followed by the nanoMIP polymerization based on the work of Canfarotta *et al.*[12] It was tested if the template, after being flown over the cell, attach the QCM surface. Moreover, nanoMIPs were tested for their ability to bind to VEGF. To create the interface, different concentrations were tested, to check their influence on the system.

2. Background and importance

2.1 Vascular endothelial growth factor (VEGF)

VEGF is part of a gene family of cysteine cross-linked homodimeric growth factors, which are divided in VEGF- A, -B, -C, -D, *orf* proteins referred to as VEGF-E, placenta growth factor (PlGF) and VEGF-F derived from a series of snake venoms. Figure 2 displays most of the family members, except VEGF-F, and the receptors they are binding to.

The mRNA transcript emanating from the gene encoding VEGF, also designated as VEGF-A, includes 8 exons which lead to the following five different isoforms after alternative splicing: $VEGF_{121}$, $VEGF_{145}$, $VEGF_{165}$, $VEGF_{189}$ and $VEGF_{206}$. The index indicates that these peptides can chemically be differentiated based on their number of amino acids. The inclusion of exon 6 and 7 is the factor that sets them apart from each other by providing the ability to bind extracellular heparin, heparan-sulfate proteoglycans and neuropilin-1 co-receptor.[13]

Within those isoforms, $VEGF_{165}$ is widely considered to have the potency to enhance vascular permeability and to act as the predominant regulator of physiological and pathological *angiogenesis*. It induces proliferation, migration and survival in endothelial cells due to its interaction with several receptors such as VEGFR-1 and -2 as well as neuropilin-1 co-receptor. It has the ability to bind to heparin, which allows 50-70% of its isoform to remain associated to cells and the extracellular matrix to regulate the bioavailability. Figure 2 depicts the crystal structure of VEGF-A in complex with one of its receptors, VEGFR-1.

VEGF family members, PlGF and VEGF-B, have been demonstrated to be non-essential during embryogenesis, however in pathological conditions PlGF synergize with VEGF-A by contributing to

angiogenesis. The expression of VEGF-C occurs within embryogenesis, whereas VEGF-D is only expressed during adult stages after birth. VEGF-E is a gene product, inducing *angiogenesis* at sites of infection on the skin, occurring in the *orf* virus. It infects especially sheep and goats but also human beings. VEGF-F, derived from *T. flavoviridis* snake venom bears strong vascular permeability activity. Interestingly, this protein is sequestered in the venom tissue, suggesting that the increase of vascular permeability is not desired within the snake body itself, but rather promoting vascular permeability within targeted animals.[14]

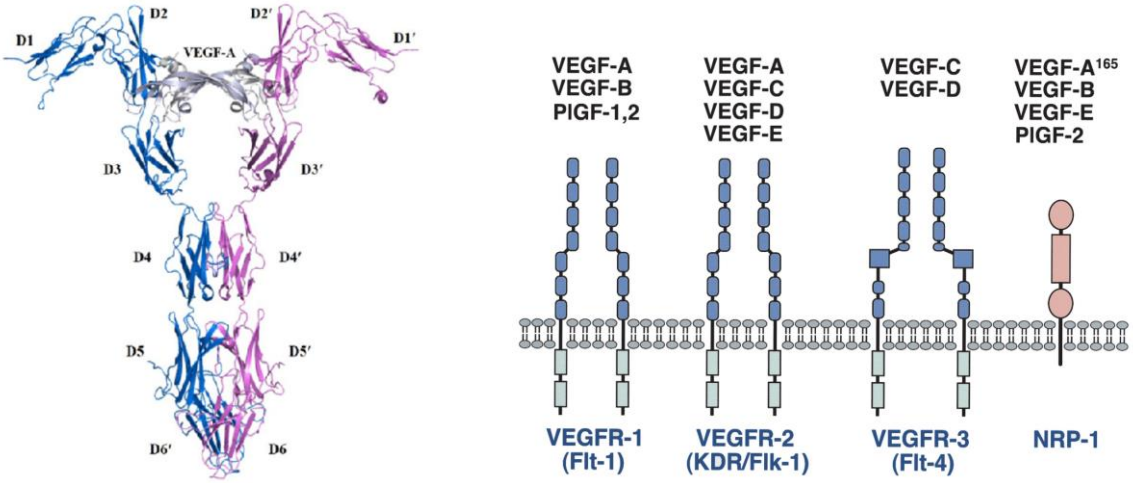

Figure 2: (Left) Crystal Structure of the VEGFR-1 extracellular domain in complex with VEGF-A. The chains of the VEGF-A homodimer are depicted in grey and light blue whereas the VEGFR-1 D1-D6 chains are in deep blue and magenta.[15] (Right) VEGF family members and the receptors they're binding to.[16]

2.1.1 Clinical significance of VEGF-A

The increase of the amount of VEGF-A in body fluids has been shown to correlate with many types of tumors including carcinomas of the breast, kidney, colon, brain, ovary, cervix, thyroid, bladder, esophagus, and prostate, and in osteoid and soft tissue sarcomas and pediatric tumors. For that reason, it is clear that it is desirable to establish a routine for monitoring its amount in body fluids. This is especially interesting for patients being either predestinated for getting cancer, or those being already in therapy, to monitor the corresponding tumor response.[16]

Yamamoto *et al.* used a sensitive enzymatic immunoassay to determine the levels of circulating VEGF-A concentrations within sera of cancer patients and healthy individuals. They demonstrated that the VEGF concentration within the sera of cancer patients showed abnormal increase compared to those of healthy participants. Overall, the study included almost 300 cancer patients, of which more than half where related to breast followed by gastric, hepatobiliary, pancreas, colorectal, lung and esophageal. The mean concentration of VEGF-A within healthy controls was determined to be 77 pg/mL whereas in comparison the highest level was 833.3 pg/mL in gastric cancer patients with peritoneal metastases. Figure 3 (left) shows the circulating levels of VEGF-A in sera of controls as well as cancer patients. Moreover, it has been shown that after breast cancer, the levels of VEGF decreased, as can be seen in Figure 3 (right).[17]

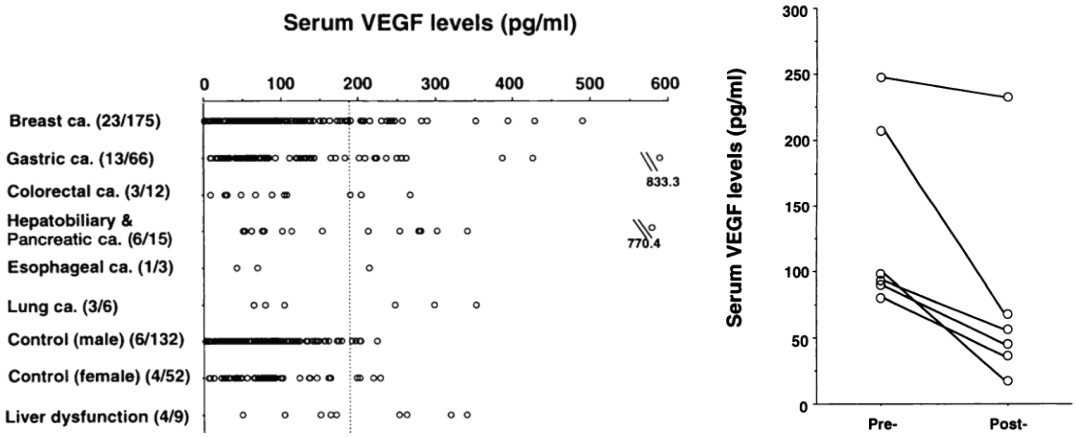

Figure 3: (left) Circulating levels of VEGF in sera in cancer patients and healthy individuals. (right) Serum VEGF levels of breast cancer patients before and after operation.[17]

For that reason, VEGF is used as a biomarker indicating regression, increased growth, recurrence, or metastatic spread in individual patients.

Although measuring VEGF-A in body fluids is more convenient compared to tumor homogenates, it has been demonstrated that the levels of VEGF-A can differ between blood serum and blood plasma from the same individuals. For example, VEGF-A is also released from platelets and leukocytes during blood clotting. In serum there was a 6 times higher amount measured compared to that of plasma. This leads to the insight that the amount of VEGF-A being measured is not necessarily only associated with tumors.[16]

2.2 (Bio-)sensors

To track and visualize physicochemical changes, which are hidden within the invisible world of microcosm, a device, termed (bio-)sensor, is used to convert a chemical change into an adequate signal. By taking advantage of its inherent, physical, measurable characteristics it helps to make objective statements about its current state. Alterations within the system lead directly to changes in the output.

A sensor, Figure 4, comprises of three parts including a sensitive layer, a transducer, and a detection unit. The first serves as a platform where physical or chemical interaction with the analyte occur. In case of a biosensor enzymes, antibodies or a (biomimetic) receptor are used to recognize specifically the analyte of interest by noncovalent interactions, leading to a certain change of chemical/physical properties. To extract a response, as a result of recognition, a stimulus is needed whose inherent characteristics change, depending on the physicochemical changes occurring during recognition. A transducer, then, assesses those changes and converts them into a measurable signal which can further be read out by a signal processing element.[18]

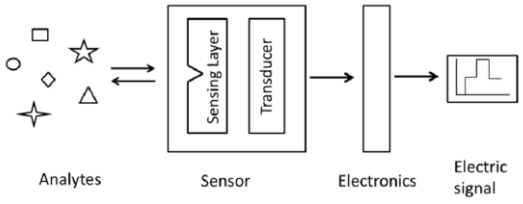

Figure 4: Schematic illustrating the fundamental components of a chemical sensor.[19]

2.2.1 Bio-interface and bioconjugation techniques

To detect the biomolecule of interest, a (bio-)interface is first needed to attach the recognition element. For this purpose, a common approach is to submerge a gold - or silver - coated surface into a thiol solution to generate self-assembled monolayers (SAM). Since the interaction between a noble metal and thiol-groups is very strong, this method offers an easy way to attach the recognition element on terminal hydroxy or carboxy functionalized thiol-alkane chains, which can be seen in Figure 5. Another approach to conjugate the analyte is achieved by modifying the surface with avidin, streptavidin or neutravidin molecules. For this purpose, the analyte must carry at least one biotin residue, to ensure binding between one of the three analogues and biotin.[20]

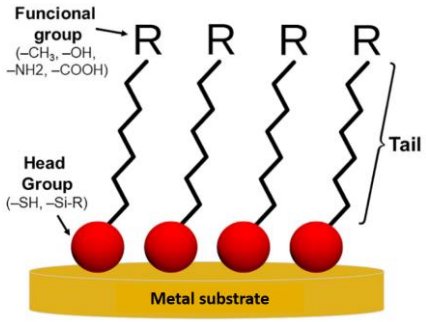

Figure 5: An illustrative representation of a conventional self-assembled monolayer (SAM) formed by an alkanethiol derivative on a metal surface. Adapted from[21].

2.2.2 Self-assembled molecules

Since metal substrates such as gold and silver tend to adsorb proteins and other molecules, leading to loss of bioactivity, it is crucially important to avoid unspecific binding on the noble metal surface. Thus self-assembled monolayers minimize irrelevant signals deriving from unspecific binding and additionally allow for immobilizing functional groups. These form a linker that the analyte can attach to or be derivatized for further surface modifications, as mentioned previously.[22]

2.2.3 Avidin, Streptavidin and Neutravidin

The three proteins Avidin, Streptavidin and Neutravidin are structural and functional analogues exhibiting high binding affinity towards biotin. Avidin and Streptavidin occur naturally, whereas neutravidin is a chemically modified version of avidin lacking its glycosylation. Even if those three proteins share high affinity to biotin and have a similar tetramer structure, they differ physically and chemically. The high pI of avidin at physiological pH (pI ~ 10) makes it less attractive in some assays. It shows enhanced non-specific binding to negatively charged molecules and surfaces, such as silica and cell membranes. In contrast, the nearly neutral charge of neutravidin prevents it from those undesirable interactions. Moreover, the neutravidin-biotin interaction is often preferred over the streptavidin-biotin one since it shows higher positive cooperativity.[23] Furthermore, Neutravidin is more stable at high pH than streptavidin. It also shows higher resistance against denaturants, which is especially important in assays demanding harsh conditions.[24] Figure 6 shows the ribbon diagram of neutravidin , as well as its conformation, when carrying two biotin molecules in its pockets.[25]

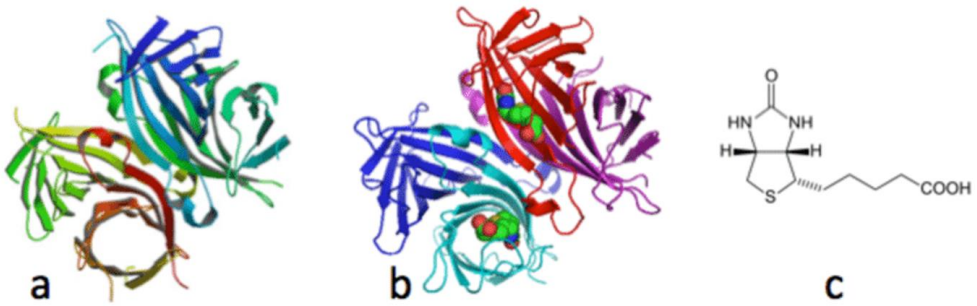

Figure 6: (a) Tetrameric structure of neutravidin. (b) Tetrameric structure of neutravidin bound to two biotin molecules. (c) Chemical structure of a biotin molecule also known as vitamin B7. [25]

2.3 Molecularly imprinted polymers (MIPs)

The term molecularly imprinted polymers refers to the template-assisted synthesis of biomimetics. This technique allows for producing polymers exhibiting high affinity towards a chosen template molecule by copolymerizing monomers and crosslinkers in the presence of a target analyte. After polymerization is completed, the template is extracted; the remaining material contains complementary cavities being ready for rebinding (

Figure 7).

For that reason, MIPs act as artificial antibodies by displaying high affinity and specificity for the targets used during synthesis. Due to their molecular structure *i.e.*, being polymers, MIPs show some advantages compared to their natural counterparts, including resistance against extreme pH, temperature, tolerance to solvents, robustness, and processability.

Replacing antibodies by MIPs seems to be a promising way to overcome the difficulties antibodies implicate. Nevertheless, during the polymerization process an antigen is exposed to conditions, *i.e.* temperature, solvents, concentration of monomers, pH change etc., which make it difficult to keep its innate folding intact. For that reason, it is very challenging to imprint proteins, nucleic acids, viruses, bacteria or cells. In contrast the imprinting of small molecules has been investigated and there are protocols existing which allow their reliable synthesis. [26]

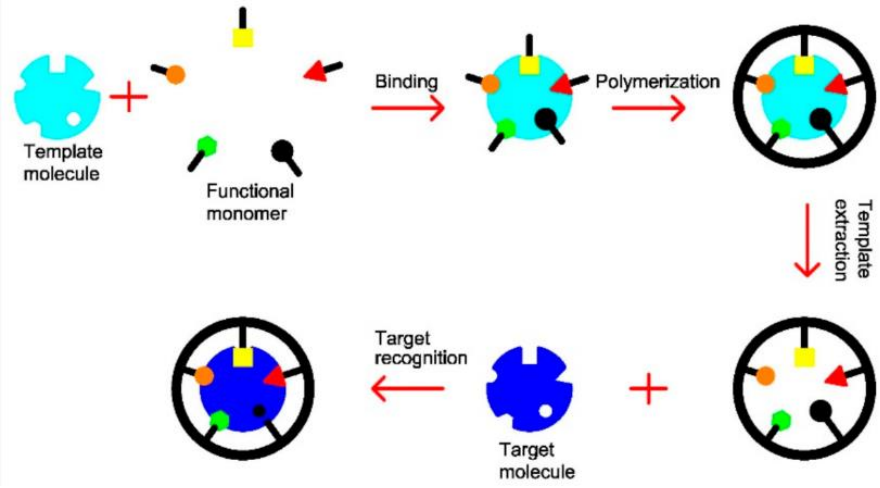

Figure 7:Synthesis of molecularly imprinted polymers. Adopted from [27].

2.3.1 Epitope imprinting

Studies about protein-protein interactions revealed that only a defined part of the protein surface is involved in recognition and binding[28,29]. For that reason, it is remarkable that the resulting interaction appears to be strong enough for achieving dissociation constants in the picomolar range. Such strong binding results from non-covalent interactions such as electrostatic interactions, hydrogen bonds and Van der Waals forces. Surprisingly, antibody-antigen binding relies mainly on the additivity of hydrophobic interactions and π-π stacking. Moreover, the areas, where hydrophobic interactions are active create a water-free environment characterized by low dielectric constants. Those lead to a strong driving force to keep the proteins even more strongly bound. Based on these findings, Rachkov suggested the idea of epitope imprinting in 1999.[30] Instead of imprinting the whole sequence of an antigen it's sufficient to imprint only that fragment that is actually involved in the binding process - the epitope.

However, it is crucial that the conformation of the epitope remains stable throughout the MIP synthesis. Any conformational change of the epitope can hinder its binding to its target, as the folded state of a protein or an epitope is vital for successful binding. For that reason, it is necessary to have a closer look on the structure of the natural epitope. They can be found in turns and loops of the protein structure, either in a conformational manner, or in a continuous or discontinuous manner. The latter emanates from the natural 3D structure of a protein, which leads to epitopes consisting of amino acids not being direct neighbors. For the imprinting process the continuous sequence of amino acids suits better, compared to the discontinuous one.

Moreover, the sequence should feature at least 5 amino acids and at most 30. Other characteristics the ideal epitope-template should offer are: resistance against polymerization conditions as well as its easy synthesis to reduce costs.

It is worth mentioning that each kind of epitope requires adjusting the imprinting process. The position and the configuration of continuous epitopes within a protein play an important role during selection. Figure 8 shows the different ways an epitope appears, including terminal- and internal- peptides. Moreover, the epitopes can be part of the secondary structure a protein exhibits such as α-helix or a β-strand.

Finally, when planning to imprint an epitope, its orientation has to be taken into account, since rebinding is only possible when the cavities in the MIP fit to its target. Apart from epitope placement and structure it should bear a signature of its parental's protein, ensuring selectivity of the binding site.[26]

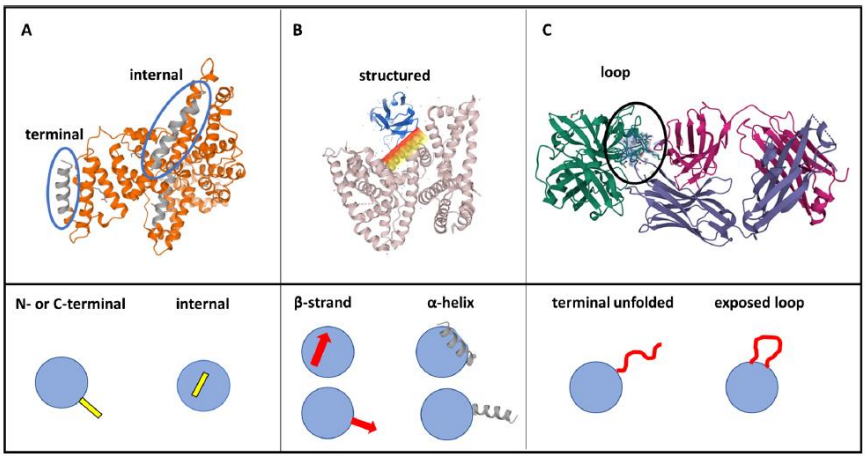

*Figure 8: (**A**) Epitopes appearing terminal or internal within a protein. (**B**) The epitopes are part of the secondary structure of its protein. (**C**) The accessibility of the epitopes might be covered due to its structure. [26]*

2.3.2 Strategies for imprinting epitopes

As mentioned above, the structural differences in epitopes require different protocols to enable their imprinting. The following paragraphs introduce three different methods for either linear or structured epitopes.

The “In solution” method enables imprinting of the epitope in a straightforward way, where the template peptide as well as the monomers and the crosslinker are all brought together, and the polymerization takes place. Although this method is easy to perform, the lack to control the stamping process leads to undesirable, heterogeneous binding sites.

Titirici *et al.* [31]was the first group proposing a concept in which the epitope is immobilized on a solid support, leading to directional imprinted binding sites. However, this method requires coupling chemistry to immobilize the epitope as well as adapting the MIP synthetic protocol to the coupling steps.

The third strategy combines both, but considers the fact that proteins are surrounded by many other molecules in their natural environment. Thus, an epitope does not only occur with a directional organization but also with a stereochemical one. For that reason, this strategy aims to imprint conformations of artificially synthesized linear epitopes to mimic the native conformational epitope by inducing a helix structure.[26]

2.3.4 Selecting the VEGF-A epitope template

To generate MIPs showing high affinity to VEGF, it is crucial to select an appropriate amino acid sequence. For this purpose, the present thesis has relied on the structural and functional studies of the receptor binding domain of VEGF based on the work of Muller *et al.* [32,33] which identified the 8-109 fragment to be involved in binding to its receptors VEGFR1 and VEGFR2. As already mentioned above, the ideal epitope should consist of at least 30 amino acids. For that reason, the work of Fuh *et al.*[34] was helpful to choose a sequence being a promising candidate for the synthesis of MIPs with high binding affinity to VEGF. They investigated three antibodies which are compatible to VEGF. Furthermore, they carried out extensive alanine-scanning mutagenesis to identify those amino acids that are unconditionally necessary for binding. Among others, they used the monoclonal antibody A4.6.1 originating from hybridoma technology when immunizing mice with human VEGF[35], whereas the two other antibodies, named G6 and B20-4, derived from a synthetic antibody library [36].

VEGF residues	Relative affinity ($EC50_{ala\ mut}/EC50_{wt}$)				
	G6	B20-4	VEGFR1	VEGFR2	A4.6.1
WT	1.0	1.0	1.0	1.0	1.0
E30	0.8	· 3.1			
I43	1.0	1.2		5.6	1.2
Y45	3.7	1.1		1.6	· 2.2
I46	2.2	1.3	· 4.0	NB	2.1
F47	3.5	1.8	3.0	3.6	1.1
K48	·· 0.3	·· 1.0	·· 1.0	0.7	· 0.7
P53	1.7	0.8			
Q79	0.7	· 0.9	· 3.0	NB	· 0.7
M81	·· 1.3	·· 1.8	·· 6.9	2.0	·· NB
R82	1.3	1.3		0.6	·· 3.3
I83	·· 40	· 0.9	·· 5.4	100	· 1.0
K84	0.8	1.5		2.2	· 1.8
P85				5.0	1.0
H86	·· 7.1	0.8	· 1.0	1.3	·· 1.9
Q87	· 2.3	1.1		1.8	··· 1.3
$G88^S$	· 2.7	1.1		1.0	·· NB
Q89	··· 92	·· >100	·· 1.0	2.5	··· NB
H90	· 1.0	1.2		1.7	··· 1.8
I91	·· 6.9	· 1.3	· 1.0	1.0	··· 1.2
G92	0.9	1.4		1.2	·· 8.5
E93	2.9	1.2		0.5	··· 6.6
M94	1.0	1.1		2.8	·· NB
V14	1.1	1.2		1..8	1.5
K16		·· 0.8	· 1.8	1.1	1.2
F17	·· >100	·· >100	·· 45	NB	1.2
M18	·· 4.4	··· >100	··· 56	5.0	1.2
D19	1.0	··· >100		0.6	0.7
Y21	··· 33	··· >100	··· 123	2.8	2.6
Q22	·· 7.2	··· 0.5	·· 11	2.2	1.4
R23	1.2	··· 9.0		1.5	1.3
Y25	·· 21	··· >100	··· 17	1.7	1.2
C26	nd	·· nd	·		
$H27^R$	0.8	· 0.1	·		
C61	nd	· nd	·		
N62	0.5	· 1.7	·	2.0	2.2
D63	·· 5.2	· 1.7	·· 7.2	0.5	0.9
E64	· 2.4	1.7	5.0	8.5	1.7
$G65^A$	0.6	1.6	· 1.0	1.3	1.7
L66	·· 0.7	· 1.8	··· 47	0.3	1.6
$N100^S$	0.9	· 1.1			1.6
$K101^R$	1.1	·· 1.0	1.0		
E103	0.7	· 1.0	· 1.0	1.1	2.3
C104	·· nd	·· nd	··		
R105	1.6	nd	· 1.0	0.8	1.4
P106	·· 2.1	0.9	· 1.0		

Figure 9 displays the relative affinities (EC_{50}) toward those antibodies and VEGFs receptors after mutating selected residues of the 8-109 fragment of VEGF to alanine (ala mut). The residues being selected in this study are all surface exposed with those in the top half emanating from one VEGF monomer and those in the lower half originating from the second monomer to form one pole of the VEGF dimer. Moreover, the crystal structure of VEGF in complex with B20-4-Fab as well as the structure of G6-Fab were used to identify those determinants being responsible for high affinity binding. Finally, they demonstrated that the original VEGF receptor VEGFR1 binds at the similar hotspot as the synthetic antibodies do.[34]

Since the exchange to alanine of most of the residues in the fragment 17-25 led to severe loss in binding affinity we concluded them to be the mainly responsible ones for binding. For that reason, we decided to imprint an epitope with the sequence H-KFMDVYQRSYC-OH. The chosen epitope allows for selective immobilization either via cysteine (aa 26 – SH group) or lysine (aa 16 – NH_2 group), while the core motif remains unchanged for the imprinting process. Figure 10 shows a representation of a α-helix structure with an amino- and thiol residue.

Figure 9: Relative affinities of VEGF towards the synthetic antibodies G6 and B20-4 as well as the monoclonal antibody A4.6.1 and the VEGF receptors VEGFR1 and VEGFR2. If the values of the relative affinities are >1 the binding is reduced when compared to the VEGF wild type. Values >4 are highlighted yellow, >10 orange and >20 red. Those amino acids being highlighted in green differ between human and murine VEGF, whereas the letters in the superscripts correspond to the sequence in mouse. [34]

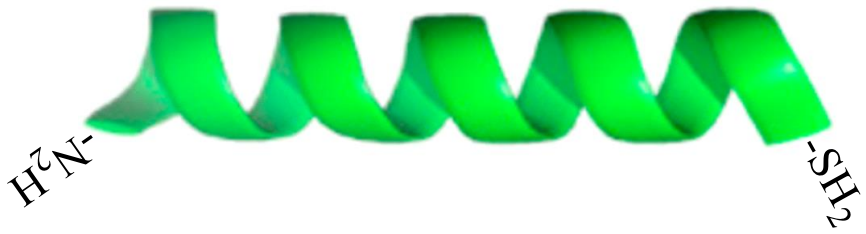

Figure 10: Representation of a α-helix structure with amino- and thiol residue. Adopted from [37].

2.4 Transducers

Depending on the characteristic to be measured there are different transducers. Within an optical sensor the transducer measures a change in either the amplitude, phase, frequency, or polarization of light. In contrast, to measure changes in mass, an electrical signal of a specific frequency is required, which causes a quartz crystal to vibrate.[38] Finally, the determination of glucose in blood represents an example of electrochemical sensors. Changes of the current are measured and transduced into an electrochemical signal.[39]

2.4.1 Surface plasmon resonance (SPR)

The principle of SPR was first documented by Wood *et al.,* who observed a new phenomenon regarding diffraction of light.[40] Biomolecular interactions cause changes in the refractive index on the layer of a metal surface. The SPR instrument detects those changes by means of the polarized laser light. It is directed towards the metal surface, and its reflection varies depending on the refractive index of the solution flowing over the metal surface. Finally, any successful binding event provokes a shift in the angle of the reflected light whose magnitude is proportional to the amount of binding that has occurred. For that reason, SPR is a very valuable tool to study and understand the mechanisms occurring between proteins, proteins and ligands as well as between antibodies and their corresponding antigens. Moreover, SPR has become many attention in the field of drug discovery and diagnostics since it is an extremely sensitive technique, enabling the detection of molecules at concentrations as low as picomolar in real-time.[22]

2.4.1.1 Refraction of light

To describe the optical density a medium has, the refractive index *n* is used. It is the ratio of the velocity of light *c* in vacuum, to the velocity *v* of a medium a wave is propagating through.

$$n = \frac{c}{v}$$

Equation 1: The refractive index is described as the velocity of light in vacuum divided by the velocity the light is going through a medium.

When a ray of light is traveling from a denser medium n_1 towards a less dense one n_2, it can be either refracted or reflected depending on the angle of incidence θ, as can be seen in Figure 11. There are three options of how the ray of light behaves: it can be refracted $\theta_1 < \theta_c$,travel along the interface $\theta_1 = \theta_c$ or it can be total internal reflected $\theta_1 > \theta_c$. Snell's law, Equation 2, explains this correlation between angles and indices of refraction.[41]

$$n_1 sin\theta_1 = n_2 sin\theta_2$$

Equation 2: Snell's law [41]

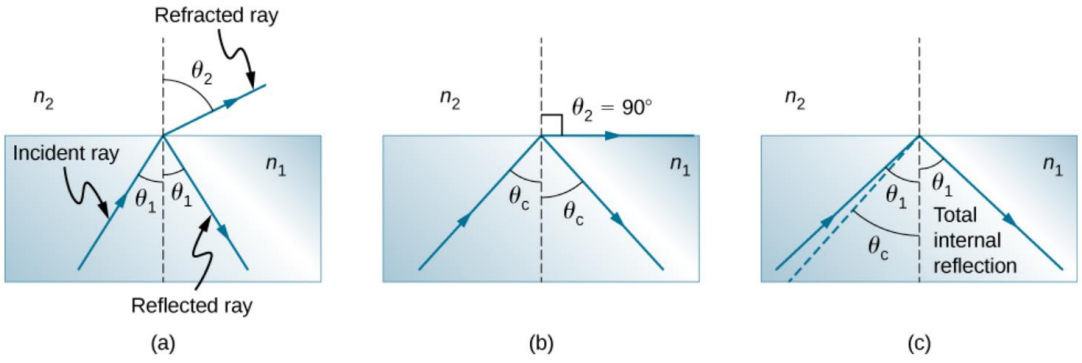

Figure 11: When the index of refraction decreases after a ray of light travels from one medium into another, the ray can be a.) refracted $\vartheta_1 < \vartheta_c$, , b.) travel along the interface $\vartheta_1 = \vartheta_c$, or c.) total internal reflected $\vartheta_1 > \vartheta_c$. Adopted from [41].

2.4.1.2 Surface plasmons and their excitation by light

Surface plasmon waves (SPW) are collective oscillations of electrons propagating along a metal-dielectric interface, which are accompanied by an electric field that decays exponentially in metal as well as in the dielectric medium (Figure 12). The entity of those oscillations is termed surface plasmon.

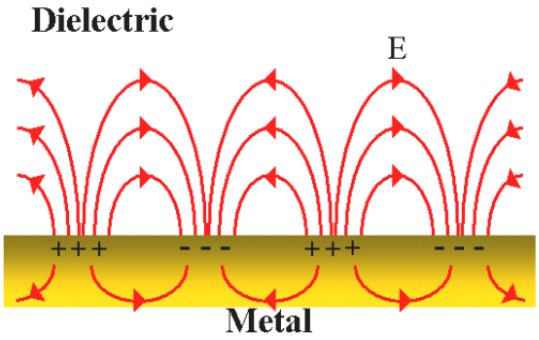

Figure 12: Schematic drawing of the electromagnetic field generated by surface plasmons. Adopted from [42].

To excite surface plasmons, one needs a transverse magnetic field or p-polarized light. The energy and the momentum of both, the incident light and the SPW, needs to be in resonance, which is also referred to as surface plasmon resonance condition. The propagation constant (K_S) of the light wave propagating through the dielectric medium is given by Equation 3. Equation 4 explains the propagation constant of the surface plasmon wave along the metal-dielectric interface. ε_m and ε_s are the dielectric constants of metal and dielectric medium, ω is the frequency of incident light and *c* is the velocity of light.

$$K_S = \frac{\omega}{c}\sqrt{\varepsilon_S}$$

Equation 3: Propagation constant of a light wave.

$$K_{SP} = \frac{\omega}{c}\left(\frac{\varepsilon_m \varepsilon_S}{\varepsilon_{m+}\varepsilon_S}\right)^{1/2}$$

Equation 4: Propagation constant of a surface plasmon wave.

To fullfill the SPR condition K_{SP} has to be equal to K_S. For that reason, a prism with high dielectric constant is used. As mentioned above, the way, incident light returns out of a prism depends on the angle of incidence. When total internal reflection occurs the incident light penetrates the medium with lower refractive index leading to attenuated total reflection (ATR). Thus, an evanescent field occur within the medium with lower refractive index. The corresponding evanescent wave propagates along the interface and its amplitude decays exponentially with distance from the interface in the less dense medium.

The evanescent wave propagation constant is given by Equation 5, where ε_p denotes the dielectric constant of the prism and θ the angle of light incidence. Using a prism with higher dielectric constant leads to higher propagation constant of the evanescent wave. This can be made equal to propagation constant of the surface plasmon wave to satisfy the surface plasmon resonance condition (Equation 6).

$$K_{ev} = \frac{\omega}{c}\sqrt{\varepsilon_p}\sin\theta$$

Equation 5: Propagation constant of an evanescent wave.

$$\frac{\omega}{c}\sqrt{\varepsilon_p}\sin\theta_{res} = \frac{\omega}{c}\left(\frac{\varepsilon_m \varepsilon_S}{\varepsilon_{m+}\varepsilon_S}\right)^{1/2}$$

Equation 6: Condition for surface plasmon resonance.

It was Otto *et al.* who firstly proposed to couple the metal with a prism. However, his configuration is difficult to control, since the dielectric is between the metal film and the prism. For that reason, the method of Kretschmann is prevailed. Kretschmann developed a configuration (Figure 13) in which the prism is coated with a thin metal layer, usually gold or silver (typically around 50 nm). That is in direct contact with the medium of lower refractive index, facilitating the generation of the evanescent wave

at the prism-metal interface. To excite surface plasmons the light needs to enter with a specific wavelength at a particular angle θ_{res}, thus fulfilling the SPR condition by matching the wave vectors of both, surface plasmon wave and evanescent wave.

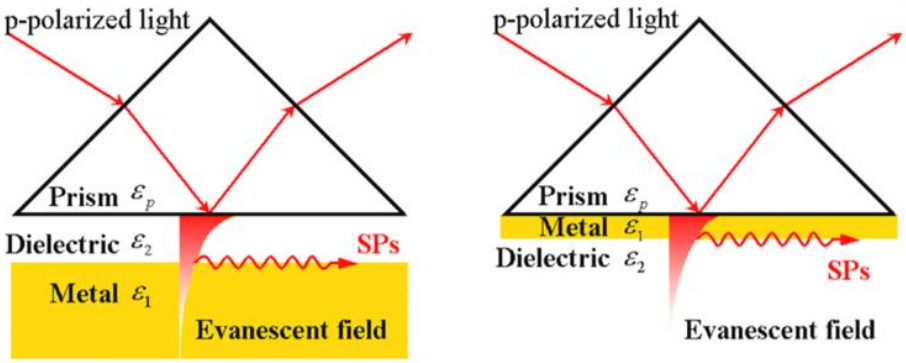

Figure 13: (left) Otto and (right) Kretschmann configuration of the attenuated total reflection method for the excitation of surface plasmons. Adopted from [42].

When surface plasmons absorb the incident light, this reduces the intensity of the reflected light. Figure 14 shows the intensity of the reflected light as a function of the angle of incidence θ at a specific wavelength. The angle of incidence leading to minimum transmission is called the resonance angle, which can be observed as a sharp dip in the diagram.

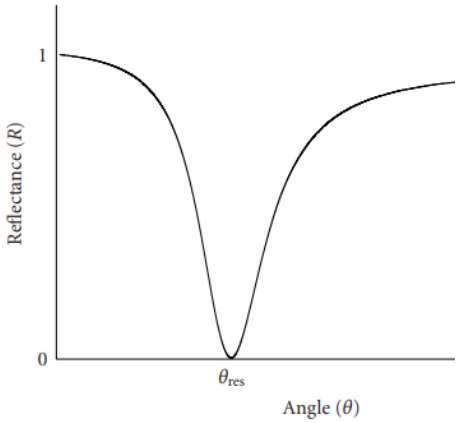

Figure 14: Intensity of reflected light depending on the angle of incidence ϑ.[43]

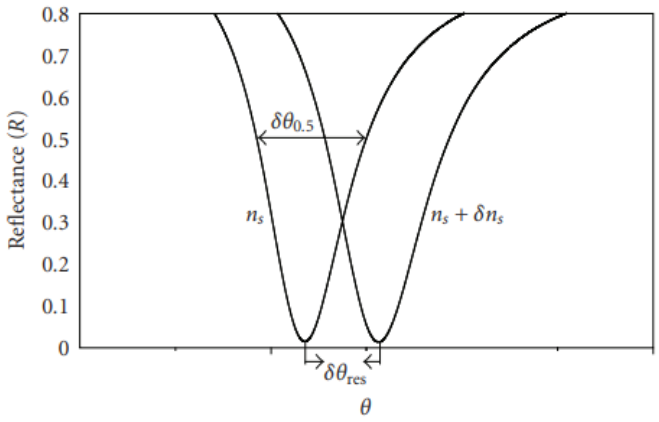

Figure 15: Changes in refractive index lead to a change in the angle of incidence to be needed to enable SPR condition[43]

The resonance angle depends on several parameters, as can be seen in Equation 6. When performing a SPR experiment, the refractive index *n* of the dielectric medium changes upon binding of analytes. This shifts the respective resonance angle. Figure 15 shows the corresponding shift occurring after the attachment of an analyte. Hence, a SPR sensor allows for assessing changes in refractive index (RI) of the medium at the SPR sensing surface. The signal of the physicochemical binding event is thus converted into a signal, namely a change in resonance angle.[43]

Since SPR sensors are very sensitive to changes in RI (approx. 10^6 nm/RIU), SPR responses are frequently recorded as a shift in RIU.[40] Depending on the respective measuring signal the SPR sensors are classified as sensors with angular, wavelength, intensity, phase, or polarization modulation.

2.4.1.3 Direct sandwich enzyme-linked immunosorbent assay (ELISA) combined with Surface Plasmon Resonance (SPR)

A direct sandwich enzyme-linked immunosorbent assay is used to detect and quantify the amount of an antigen in a sample of interest. The term sandwich refers to the nature of the assay, where the antigen is sandwiched between two antibodies, as can be seen in Figure 16. To detect the target of interest *i.e.*, the antigen, it is crucial to use antibody pairs. The primary antibody, also called capture antibody is immobilized in a first step on a solid surface. The antigen is then added to bind to it via its epitope followed by an incubation period. In the final step a detection antibody is added, which has to bind to another sequence of the antigen, to complete the sandwich. The following detection depends on the label of the detection antibody. When being labeled with an enzyme, the addition of a corresponding substrate is necessary to provoke either a colorimetric or a fluorescent reaction. In comparison, labeling with a fluorophore is more convenient, because the emitted light can be detected directly and is proportional to the amount of antigen. This makes it possible to calibrate the respective sensor in a rather straightforward manner.[44] However, it is also possible to use SPR to detect binding events in ELISA.

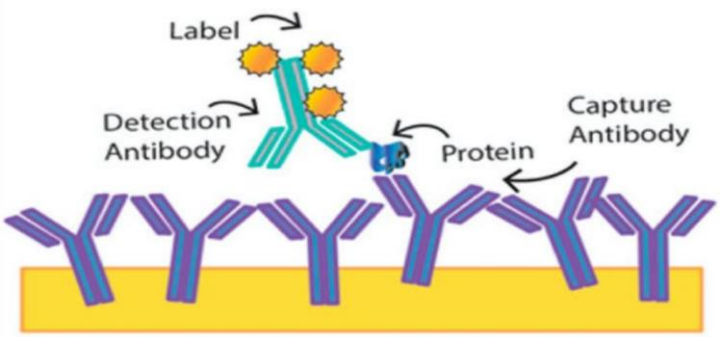

Figure 16: Direct Sandwich ELISA. Firstly the primary antibody captures the antigen, followed by the addition of the secondary antibody which carries a label, for example a fluorophore, enabling the detection.[45]

2.4.2 Quartz Crystal Microbalance (QCM)

A QCM is a transducer converting mass changes on its electrode surfaces into frequency changes and, this, into a measurable signal. It usually relies on a thin, monocrystalline, AT-cut quartz crystal. Monocrystalline SiO_2 in its α-modification contains a polar axis. Due to this characteristic, deformation occur when being exposed to mechanical stress or pressure. The shifted positive and negative charge centers do not compensate each other, resulting in a macroscopic dipole, namely surface charge. Conversely, the quartz crystal can also experience mechanical deformation when being subjected to an electric field. This feature can be harnessed to observe molecular interactions in real-time by applying an alternating electric voltage to the quartz crystal. The crystal then vibrates with a natural resonant frequency which changes when molecules or mass is added. This results in a shift of the frequency which can be detected and quantified. Equation 7 gives the relation between the change in frequency and change in mass. The phenomenon of the duality between mechanical and electrical responses in certain materials is called the piezoelectric effect.[38,46]

$$\Delta f = -\frac{2f_0^2 \Delta m}{A\sqrt{\rho_q \mu_q}}$$

Equation 7: Sauerbrey Equation. Δf… Frequency change [Hz], Δm… Mass change [g], ρ_q… Density of the quartz [g/cm^3], A… Cross-sectional area of the crystal [cm^2], f_0… Resonant frequency [Hz], μ_q… Shear modulus of the quartz [g/cm s^2]

Figure 17 depicts the QCM sensor which is constructed AT-cut using quartz crystals with integrated metal electrodes as its primary material. To facilitate the detection of the target analyte, a responsive coating material is applied to the sensor surface. Additionally, an electronic circuit is essential for converting the measured quantity into an electrical signal.

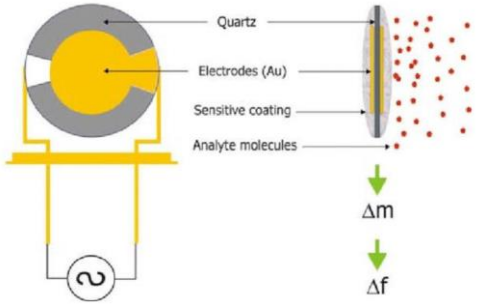

Figure 17: Fundamental operating principle of the Quartz Crystal Microbalance (QCM) sensor.[47]

3. Experimental

3.1 Materials

The following tables summarize a list of the chemicals and materials used for the experiments in this thesis.

Analyte immobilization	
Chemicals	**Supplier**
Silica gel 60 (63-200 µm, 70-230 mesh)	Merck
NaOH	Emsure
3-Aminopropyl)triethoxysilane (APTES)	Sigma Aldrich
Glutaraldehyde (50%)	Amresco
PBS-buffer (NaCl, KCl, Na_2HPO_4, KH_2PO_4, DI H2O), pH 7.4	See below
NaCl	AppliChem
KCl	VWR
Na_2HPO_4	Emsure
KH_2PO_4	Merck
H-KFMDVYQRSYC-OH	Peptides & Elephants
Anhydrous toluene	Sigma Aldrich
Materials	
Reflux condenser	
Oil bath (105°C)	
Round bottom flask	
Magnetic stirrer	
Vacuum pump	
Sintered disc filter funnel (type 1)	
15 mL Falcon Tubes	
Rotator Revolver	

Table 1: List of chemicals and materials for analyte immobilization.

NanoMIP Polymerization	
Chemicals	**Supplier**
Functionalized silica gel from previous step	-
Argon	Messer
BIS	Alfa Aesar
NIPAm, 97 %	Alfa Aesar
AA	Merck
APS, 98% extra pure	Acros Organics
TEMED	Alfa Aesar
Double distilled water (MQ water)	Milli Q
EtOH	Fisher Scientific
Materials	
Polymerization vial (15 mL, sealable glass vial)	
Needle: ϕ 0.90 x 50 mm for Ar purging	
SPE-cartridge with 100 µm PE porosity frit	
Water bath (65°C)	
Thermostat	
Heating plate	
Ice bath (0°C)	
Ultrasonication bath	

Table 2: List of chemicals and materials for NanoMIP polymerization.

QCM functionalization	
Chemicals	**Supplier**
EtOH abs.	Fisher Scientific
Cysteamine	Tokyo Chemical Industry (TCI)
Butanethiol	Sigma Aldrich
Human Serum Albumine	Sigma Aldrich
Materials	
Quartz blanks: Freq.: 10000 ± 30 kHz, Dia.: ϕ 13.8 + 0 /- 0.05 mm, Bevel: R 60 mm; 0.5-0.6 mm	
Disposable syringe, 1mL, non-sterile, PP	
Needle: ϕ 0.90 x 50 mm	
Small petri dishes	
Plasma cleaner	
Pasteur pipette	

Table 3: List of chemicals and materials for QCM functionalization.

On-chip kinetic measurements	
Chemicals	**Supplier**
PBS (NaCl, KCl, Na_2HPO_4, KH_2PO_4, DI H2O), pH 7.4	VWR
Tween	Sigma Aldrich
Neutravidin	Fisher Scientific
Human VEGF-165 Recombinant Protein expressed in P. pastoris	Fisher Scientific
VEGF165 human recombinant, expressed in E. coli	Sigma Aldrich
Anti-VEGF Antibody, Alexa Fluor® 647 Conjugate from rabbit	Sigma Aldrich
Biotin Anti-VEGF 165A antibody (ab271201)	Abcam
Recombinant human Interleukin-6 (ab198571)	Abcam

whole human blood	Innovative Research
Sucrose	Sigma Aldrich
Glycin	Sigma Aldrich
HCl	Sigma Aldrich
NaOH	Sigma Aldrich
EtOH	Sigma Aldrich
$MgCl_2$	Sigma Aldrich
Nuclease free water	Sigma Aldrich
Bovine Serum Albumine	New England Biolabs
Materials	
Petri dishes	
freezer	
Falcon tubes	
Laminar Flow Bench	
Cooling box	

Table 4: List of chemicals and materials for SPR measurements.

Preparation of biosensor chips	
Chemicals	**Supplier**
Hellmanex	Hellma Optics
MilliQ water	MilliQ
Chromium	MaTeck
Gold	MaTeck
PEG-OH	ProChimia Surfaces
PEG-Biotin	ProChimia Surfaces
Materials	
Plasma Cleaner	
Pasteur Pipette	
DC-chambers	

Table 5: List of chemicals and materials for the preparation of biosensor chips.

3.2 Instruments

- Scanning Electron Microscope from Zeiss Gemini SUPRA 55VP
    - Software: SmartSEM
- Dynamic Light Scattering: Malvern Zetasizer nanoseries
    - Software: Zetasizer
- Ultrasonic bath from Elma S120 Elmasonic
- Thermostat Ikatron ETS IKA Labortechnik
- Thermostat EKT Hei-Con Heidolph
- Heating plate IKA RCT basic
- Heating plate Heidolph MR Hei-Standard
- Manual Diener Zepto plasma cleaner with Balcas TCP 015 vacuum pump
- Balance sartorius
- Thermoshaker Mixer HC starlab
- Rotator Revolver Thermo Scientific

- pH meter from Metrohm
- Evaporator HHV Ltd, Auto306 Lab Coater
- QCM-measurements:
    - Universal Counter: Agilent 53131A
    - Laboratory Power Supply: EA-PS 2032-025
    - Network Analyzer: Agilent Technologies E5062A
    - Software: FreqMeas5313Xa 1.4.vi

Figure 18 shows the QCM measurement setup being used within the experiments. The power supply provides 0-15V direct current. These power an oscillator circuit, with the QCM serving as the frequency-determining component. Moreover, a two-electrode system is used. The reference electrode compensates fluctuations regarding viscosity and density occurring in liquid phase After the injection of liquid into the QCM measurement cell, the mass of the electrode increases, leading to a decrease in frequency. A frequency counter monitors this frequency, which is read out to the computer by a LabView routine.

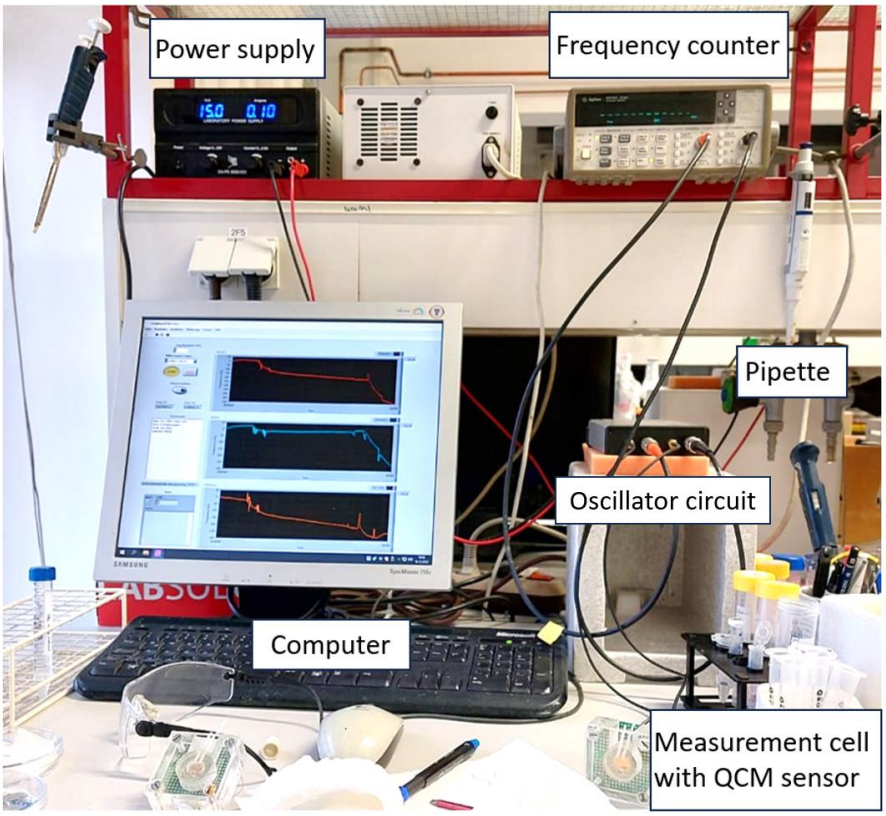

Figure 18: Setup for QCM measurement. The pipette delivers liquid into the measurement cell. With the power supply, voltage can be applied to the QCM sensor. Changes within the frequency are recorded by the frequency counter, sending these data to the computer software.

- SPR-measurements:
    - Bandpass filter (LBPF, Thorlabs, FL632.8-10)
    - Chopper (Signal Recovery, Model 197, frequency f = 933 Hz)
    - Photodiode with lock-in amplifier (EG&G, Model 5210)
    - Photomultiplier (Hamamatsu, H6240-01)
    - Photon counter (Agilent, 53131A, f = 225 Mhz)
    - Lenses (Thorlabs, focal length f = 50 mm, numerical aperture of NA = 0.2, LB1471)
    - Laser notch filter (LNF, Melles Griot, XNF-632.8-25.0M CVI)
    - bandpass filters (FBPF, Thorlabs, FB670-10 and Andover Corporation Optical Filter, 670FS10-25).

Figure 19 shows the optical set-up for the SPR measurements in Kretschmann configuration. The path of the Helium-Neon laser involves passing through the bandpass filter, followed by the chopper and the polarizer. The monochromatic beam is introduced into a prism composed of LASF9 glass (Schott, refractive index n= 1.850), securely positioned on a rotational stage and undergoes a reflection of the sensor chip. To achieve optical alignment between the sensor chip and the prism, a high-refractive-index immersion oil (Cargille Laboratories; refractive index n = 1.7000, cat. No. 1812) is applied.

To detect the beam, a photodiode, coupled with a lock-in amplifier is utilized. The emitted fluorescence light (λ_{em} = 670 nm) is collected by a photomultiplier and a photon counter. This light is detected, after passing through two lenses, a laser notch filter and two bandpass filters.

The software Wasplas (Max Planck Institute for Polymer Research in Mainz, Germany) was utilized to display the reflected beam intensity (R) as a percentage and the fluorescence intensity (F) in counts per second (cps), either with respect to time (R(t)) or the angle of incidence (R(θ)).

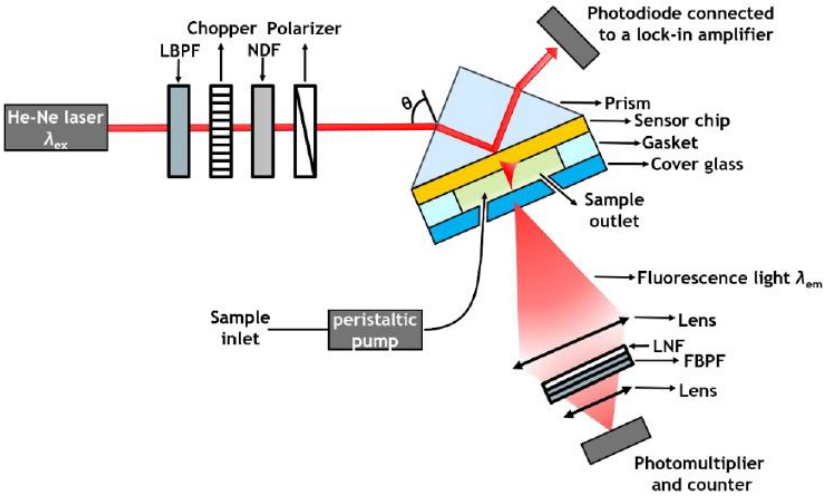

Figure 19: Schematic setup for SPR measurements. Adopted from [48].

3.3 Procedures

3.3.1 ELISA

Preparation of biosensor chips

Microscope slides made from BK7 glass were cut into pieces of approximately 25x20mm in size. These underwent a series of washing steps for cleaning them. First, they were washed with ethanol and sonicated with 1 % Hellmanex (Hellma Optics) in MQ water. Second, they were washed with solely MQ water and finally with EtOH for 15 minutes each.

The resulting glass substrates were dried with pressured air and mounted onto a sample holder followed by loading them into the evaporator. A vacuum with a pressure lower than 10^{-6} mbar was created using a combination of a vacuum pump and liquid nitrogen. Chromium was then thermally evaporated until a thickness of 2 nm was achieved. Under the same vacuum conditions, deposition of a gold layer followed until a thickness of 50 nm was reached.

To obtain SAMs on the gold chips' surface, they were incubated overnight in an ethanol solution containing a mixture of PEG-OH and PEG-biotin. Those could bind via its thiol groups to the gold surface. Finally, the slides were rinsed with pure ethanol and stored in the dark under argon preventing oxidation.

On-chip kinetic measurements

Prior to the kinetic measurements R(t), an angular reflectivity scan R(θ) was performed on the chip in contact with air at an angle range of θ = 20°-30°. Subsequently, the flow-cell was mounted and PBST (nuclease-free PBS with 0.05% (v/v) Tween20) was flown over the chip. The kinetic measurement was initiated by determining the fixed angle of the low-angle side of the resonance dip in the angular reflectivity scan R(θ) (θ = 45°-60°) in PBST. After every reaction step an angular reflectivity spectrum R(θ) (θ= 45°-60°) was recorded.

At the beginning of the kinetic measurement, Neutravidin (1.86 µM) in PBST was applied for 20 min. To capture the analyte of interest – VEGF – a capture antibody equipped with biotin (Biotin Anti-VEGF 165A antibody) was then flown for another 20 minutes. To determine any unspecific reactions, 18 nM of the detection antibody (Anti-VEGF Antibody, Alexa Fluor® 647 Conjugate) was applied for 5 min. Subsequently the analyte (Human VEGF-165 Recombinant Protein expressed in *P. pastoris*) was flown for 10 min followed by adding the detection antibody for 20 min. The results section explains further details of the respective experiments.

Finally, to calibrate the system, sucrose solutions with concentrations of 1%, 2%, and 4% (w/v) in PBST (n=1.3344, 1.3359, 1.3388), respectively, were applied at the end of the kinetic measurement. This calibration process allowed for normalizing the SPR response R(t) of individual measurements. The baseline in PBST was established as zero, allowing for converting the response into milliRefractive Index Units (mRIU).

3.3.2 MIP-QCM approach

Template immobilization on silica gel

The steps being necessary for the template immobilization are depicted in Figure 20. First, 2 g of silica gel were boiled in 4 mL 1 M NaOH for 20 min (reflux condenser in oil bath at 105°C), followed by washing steps with 0.2 L DI H_2O, 0.2 L PBS, 3 x 0.2 L DI H_2O and 2 x 0.2 L Acetone. The silica gel was then dried using a filter funnel.

Then, the activated silica was incubated in 4 mL 2.5 % (v/v) APTES solution in anhydrous toluene for 24 h at RT in a 15 mL Eppendorf tube and placed on a rotator revolver.

The supernatant was decanted onto a sintered disc filter funnel and washed with 8 x 10 mL Acetone followed by 2 x 10 mL of EtOH/Acetone (1:1).

After drying, the silanized silica gel was incubated with 4 mL of 7.5 % Glutaraldehyde solution in 0.01 M PBS (pH 7.4) for 2 h in a 15 mL Falcon tube on the rotator revolver. It was washed again with 2 x 50 mL PBS under vaccum in a sintered disc filter funnel. Due to the immobilized GA, the SG turned orange.[12]

In a last step, 2 g of SG was incubated for 12 h with 4 mL of epitope solution (0.5 mg/mL in 10 mM PBS, pH 7.4) in a 15 mL Falcon tube and placed in the fridge. The resulting, functionalized SG was washed with 10 x 10 mL DI H_2O in a sintered funnel under vacuum, dried and stored at 4 °C.

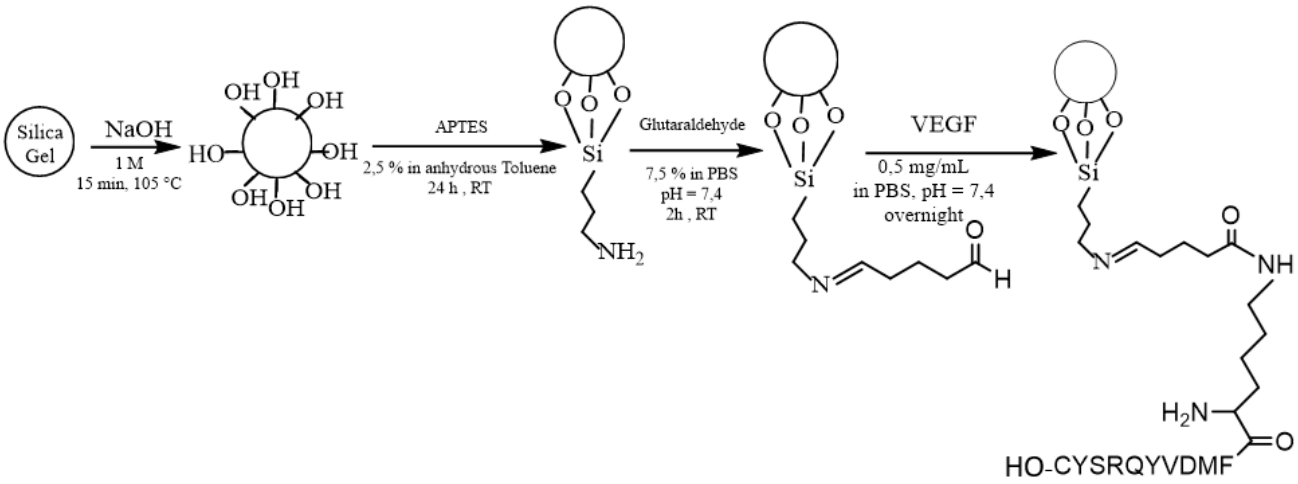

Figure 20: Template Immobilization of VEGF. Based on [12].

nanoMIP Polymerization

For the indirect approach nanoMIPs were obtained using an established protocol based on the work of Francesco Canfarotta.[12] For this purpose, two different polymerization mixtures were produced.

Polymerization mixture A contained TBAM, while B was prepared without including it. This allows for assessing if the hydrophobic nature of TBAM has an impact on the resulting nanoMIPs. Table 1-Table 5 show the compounds used as monomers and initiators, as well as recipes and final volumes to produce the polymerization mixtures.

Polymerization mixture

Chemical	Mol-%		c [µmol/mL]	
	A	B	A	B
BIS *N,N'-methylene-bis-acrylamide, $C_7H_{10}N_2O_2$*	5	5	7.4	7.3
NIPAm *N-Isopropylacrylamide, $C_6H_{11}NO$*	75	80	110.3	117.5
AA *Acrylic Acid, $C_3H_4O_2$*	10	15	14.7	22
TBAM *N-Tertbutylacrylamide $C_7H_{13}NO$*	10		14.7	

Table 6: Compounds of the polymerization mixtures A and B as well as their concentrations and Mol-%.

Stock solution for polymerization mixture A

Chemical	mass	Dissolve in	$C_{Stock\ solution}$	Volume added to polymerization mixture	c_{final}
BIS	11 mg	484 µL EtOH	22.7 mg/mL	200 µL	1.1 mg/mL
NIPAm	50 mg	250 µL EtOH	199.6 mg/mL	250 µL	12.5 mg/mL
AA	110 µL	759 µL MQ H_2O	1100 mg/mL	4.0 µL	1.1 mg/mL
TBAM	10 mg	67 µL EtOH	149.6 mg/mL	50 µL	1.9 mg/mL

Table 7: Recipe for the preparation of the stock solution of polymerization mixture A, including TBAM.

Stock solution for polymerization mixture B

Chemical	mass	Dissolve in	$C_{Stock\ solution}$	Volume added to polymerization mixture	c_{final}
BIS	11 mg	484 µL EtOH	22.7 mg/mL	200 µL	1.1 mg/mL
NIPAm	109 mg	604 µL EtOH	180.4 mg/mL	295 µL	13.3 mg/mL
AA	12.7 µL	87.9 µL MQ H_2O	127 mg/mL	50 µL	1.6 mg/mL

Table 8: Recipe for the preparation of the stock solution of polymerization mixture B.

Initiator stock solution

Chemical	mass	Dissolve in	V_{added}
APS Ammonium persulfate, $(NH_4)_2S_2O_8$	5 mg	1000 µL MQ H_2O	5 µL
TEMED Tetramethylethylene-diamine, $C_6H_{16}N_2$	5 µL	995 µL MQ H_2O	5 µL

Table 9: Recipe for the preparation for the initiator stock solution (equally for A and B).

To prepare each polymerization mixtures, glass vials with a volume of 15 mL had to be sonicated for 5 minutes in Acetone, EtOH and MQ H_2O, respectively. NIPAm, BIS and TBAM were prepared in separate 1.5 mL Eppendorf tubes and sonicated for 10 minutes each to completely dissolve the monomers. The following table shows the chemicals being added together in the glass vial followed by a vortexing and 15 minutes sonication step.

Chemical	A	B
MQ H_2O	1.986 mL	1.940 mL
EtOH	500 µL	505 µL
TFE	1 mL	1 mL
BIS	200 µL	200 µL
NIPAm	250 µL	295 µL
AA	4 µL	50 µL
TBAM	50 µL	

Table 10: Volumes of the polymerization mixtures of A and B.

Afterwards the mixtures were degassed by purging with Ar for 20 minutes each. In the meantime, the initiator stock solutions were prepared by vortexing to ensure complete dissolving.

The polymerization mixture was then added to the functionalized SG in a 15 mL falcon tube. The APS and TEMED stock solutions were added as well; then everything was degassed for 5 more minutes. In a last step the Eppendorf tubes were fixed on a shaker to polymerize for 12 h.

Affinity separation

High affinity nanoMIP particles were obtained through an affinity separation. For this purpose, the silica gel/polymerization mixture was transferred into a 15 mL extraction column equipped with a 100 µm porosity PE frit. First, the low affinity particles were eluted with 25 mL 40°C MQ H_2O. The cartridge was then placed in a fridge for 15 minutes to cool down followed by the elution of 50 mL of the high affinity particles with 20°C MQ H_2O.

To calculate the concentrations of the particles, they were weighed after elution and subsequent solvent evaporation followed by a secondary weighing. Table 11 show the concentrations obtained.

	Concentration	
	A	**B**
LA	5500 µg/mL	833 µg/mL
HA	2200 µg/mL	233,3 µg/mL

Table 11: Concentrations of high- and low affinity particles.

QCM functionalization

Before using the QCMs, they had to be cleaned for 20 minutes in a plasma cleaner. Three different functionalization mixtures were prepared to determine the optimal ratio ensuring adequate binding to VEGF as well as to the corresponding nanoMIPs. Table 12 shows the volumes and concentrations being used. The cysteamine stock solution was prepared using 7.7 mg Cysteamine dissolved in 1mL EtOH.

	1:560		**1:6000**		**1:10.000**	
	Volume added	**Final concentration**	**Volume added**	**Final concentration**	**Volume added**	**Final concentration**
EtOH abs.	9.773 mL		2.753 mL		3.480 mL	
Cysteamine Stock (100mM)	83 µL	0.8 mM	46 µL	0.8 mM	28 µL	0.8 mM
Buthanethiol	500 µL	448 mM	3 mL	4.8 M	3 mL	8000 mM

Table 12: Volumes and concentrations of the compounds being used for the preparation of the functionalization mixture.

After the cleaning step, the QCMs were placed in petri dishes, covered with the functionalization mixture and sealed with parafilm to let them incubate for 24 hours. The following day the QCMs were washed in petri dishes firstly with EtOH and secondly with PBS. After letting them dry at air they were incubated for 2 hours with 5-10 drops of 5mM GA solution which was prepared beforehand. The GA stock solution and dilution was prepared as follows:

GA stock (100 mM): 28 µL GA in 1472 µL PBS

GA dilution (5mM): 0.5 mL GA stock in 9.5 mL PBS

Again, the QCMs were washed in petri dishes filled with PBS and dried in air. The quarz which had to be incubated with analyte was marked with a dot. 5-10 µL of one of the solutions were then dropped onto the electrode. For the analyte solution the QCM was incubated for 12 hours and for the ethanolamine solution only 25 minutes were sufficient. Both solutions were prepared as follows:

Analyte solution (6 mM):

Ethanolamine solution (100 mM): 9 µL EA in 1.491 mL PBS

Figure 21 show the reaction occurring during functionalization of the QCM.

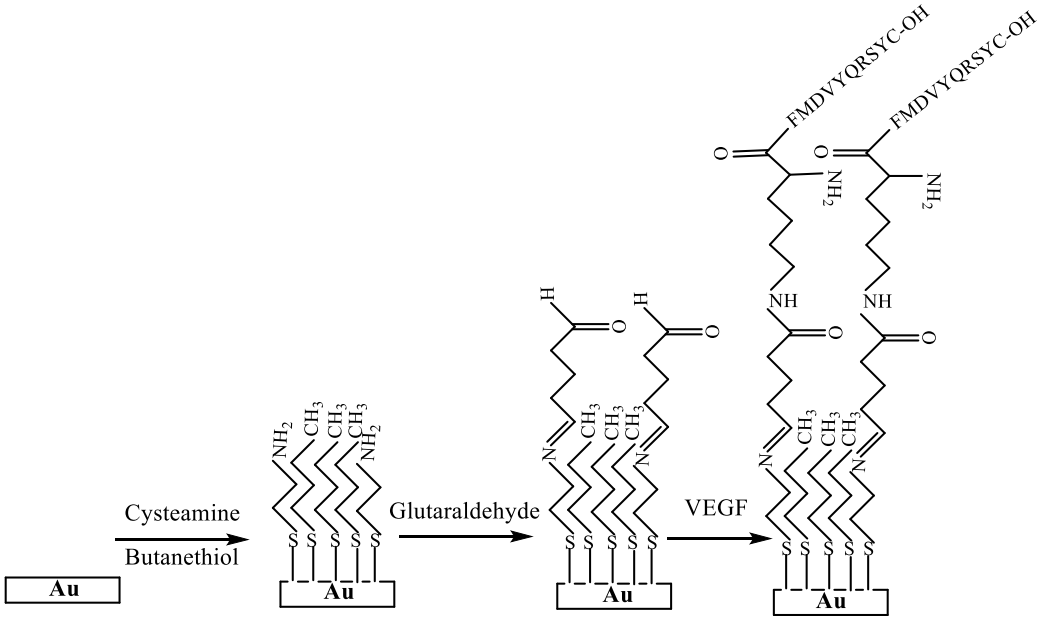

Figure 21: QCM Functionalization with Cysteamine:Butanethiol, Glutaraldehyde and VEGF

4. Results and Discussion

4.1 ELISA

Evaluation of dAb concentration via Titration (Biotin SAM 1:5)	
Chemical	**concentration**
Neutravidin	1,86 µM
Biotin Anti-VEGF 165A antibody (cAb)	6,25 nM
VEGF165 human recombinant, expressed in E. coli (Fisher Scientific)	5,2 nM
Anti-VEGF Antibody, Alexa Fluor® 647 Conjugate from rabbit (dAb)	9 nM 14,5 nM 18 nM 54 nM 90 nM

Table 13: Used chemicals and concentrations for the evaluation of dAb.

To figure out the optimal detection antibody concentration, 5 different concentrations were evaluated. Each of them was applied for 20 minutes followed by a washing step with PBST. As can be seen in Figure 22 within the fluorescence signal, only the dAb concentration of 18 nM achieved saturation within 20 minutes. For that reason, this concentration was used to titrate VEGF 165. Moreover, it was chosen since it was a good compromise to avoid too high signals from unspecific binding. The graph shows in the beginning a noticeable increase within the SPR signal after applying Neutravidin, capture antibody and VEGF 165, respectively. Table 13 shows the chemicals and concentrations being used within this experiment.

After every reaction step an angular reflectivity spectrum was recorded (Figure 23), showing the increase of the angle to be needed to fulfill the SPR condition. The red line denotes PBST, whereas the green line corresponds to Neutravidin. The blue line represents the cAb. After each step applying dAb with higher concentrations an increase within the fluorescence signal is observed. The box in the graph indicates which line corresponds to which dAb concentration.

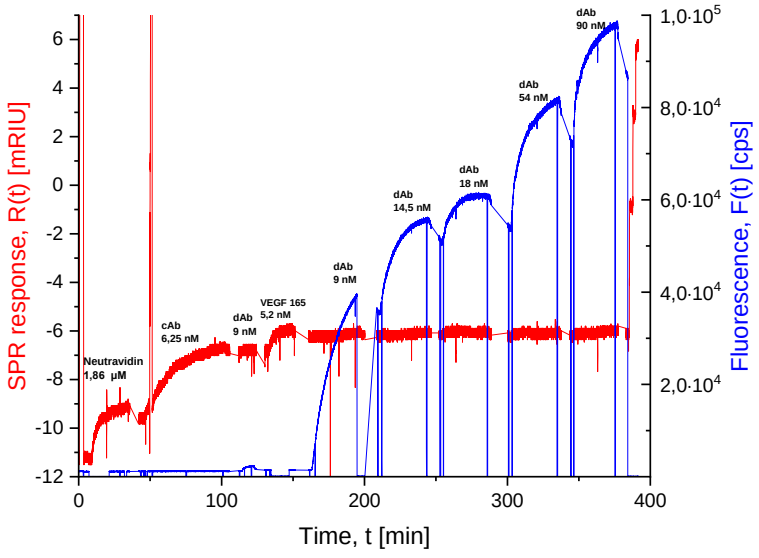

Figure 22: Evaluation of dAb concentration.

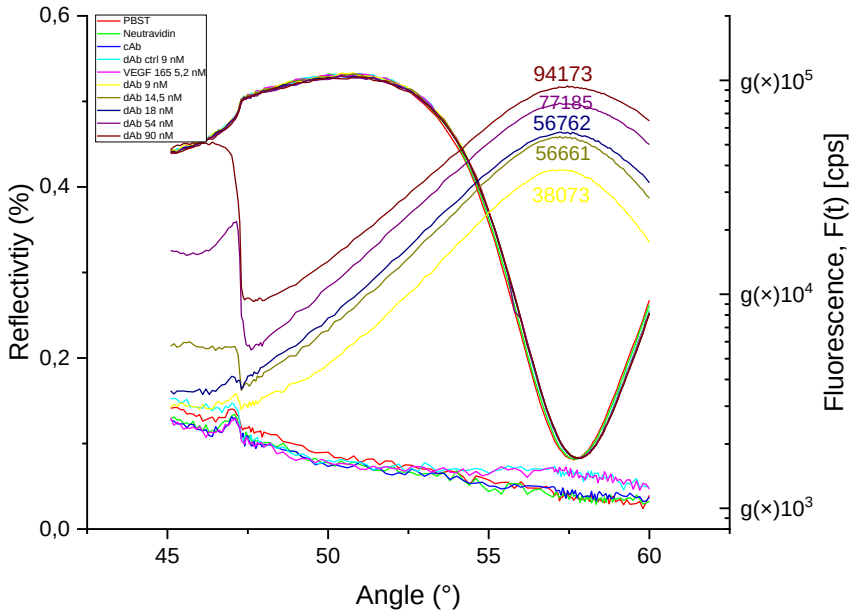

Figure 23: Corresponding angular reflectivity spectrum.

Titration of VEGF 165 (Biotin SAM 1:5)	
Chemical	**concentration**
Neutravidin	1,86 µM
Biotin Anti-VEGF 165A antibody (cAb)	6,25 nM
VEGF165 human recombinant, expressed in E. coli (Fisher Scientific)	0,0052 nM 0,052 nM 0,52 nM 5,2 nM 26 nM
Anti-VEGF Antibody, Alexa Fluor® 647 Conjugate from rabbit (dAb)	18 nM

Table 14: Used chemicals and concentrations for the titration of VEGF 165 purchased from Fisher Scientific.

Figure 24 shows the SPR measurement of the titration of VEGF 165. After applying Neutravidin for 40 minutes onto the chip, the SPR signal increased, since the latter bound to the biotin SAM. The following capture antibody (cAb) was introduced likewise for 40 minutes. Again, this results in an increase of the SPR signal due to binding between the biotin molecules linked to the cAb and Neutravidin. To ensure no unspecific binding took place, the detection antibody was applied for 5 minutes. Since the fluorescence signal did not increase notably, the lowest concentration of VEGF 165 was applied for 10 minutes followed by flowing the dAb for 10 minutes over the cell leading to an increase in the fluorescence signal. The following steps alternated between applying VEGF 165 at increasing concentrations and introducing dAb. The higher the concentration of VEGF 165, the more the fluorescence increased. Figure 25 shows the corresponding calibration curve. To determine the LOD, which is observed to 0.02 nM, a linear was fit to the data. Figure 26 depicts the shifts of the angle of incidence in the angular reflectivity spectrum occurring after a binding event. Moreover, the shifts of the fluorescence signal are represented. The red line corresponds to PBST, whereas the green line denotes Neutravidin followed by a noticeable shift elicit by the capture antibody (blue line) and VEGF 165 at 0.0052 nM (pink line). A notable increase in the fluorescence signal is observed after each

step of applying detection antibody. This increase gets more prominent with higher analyte concentrations.

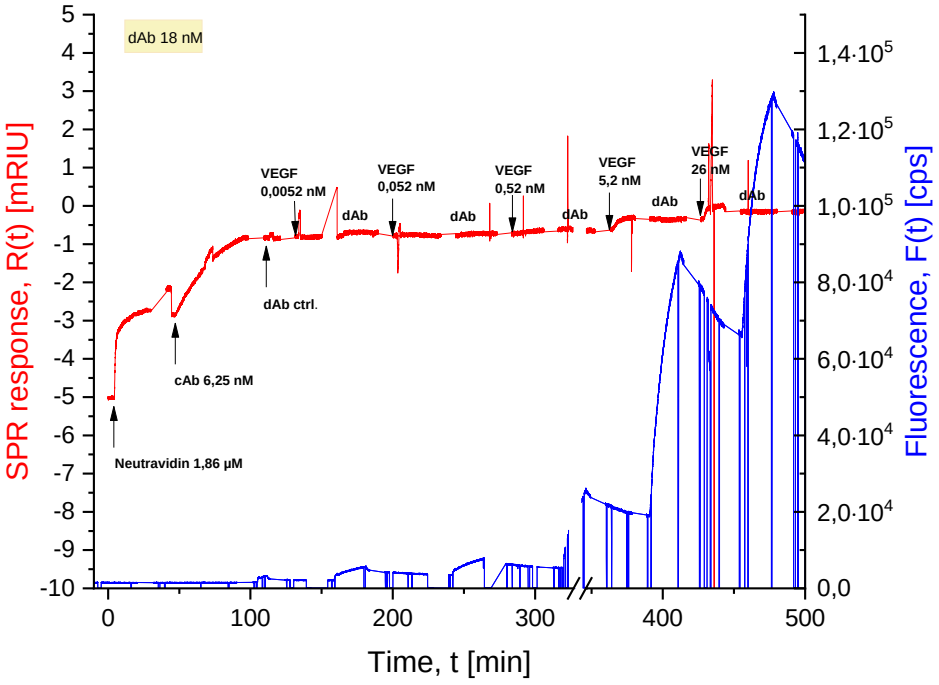

Figure 24: SPR measurement of the titration of VEGF 165.

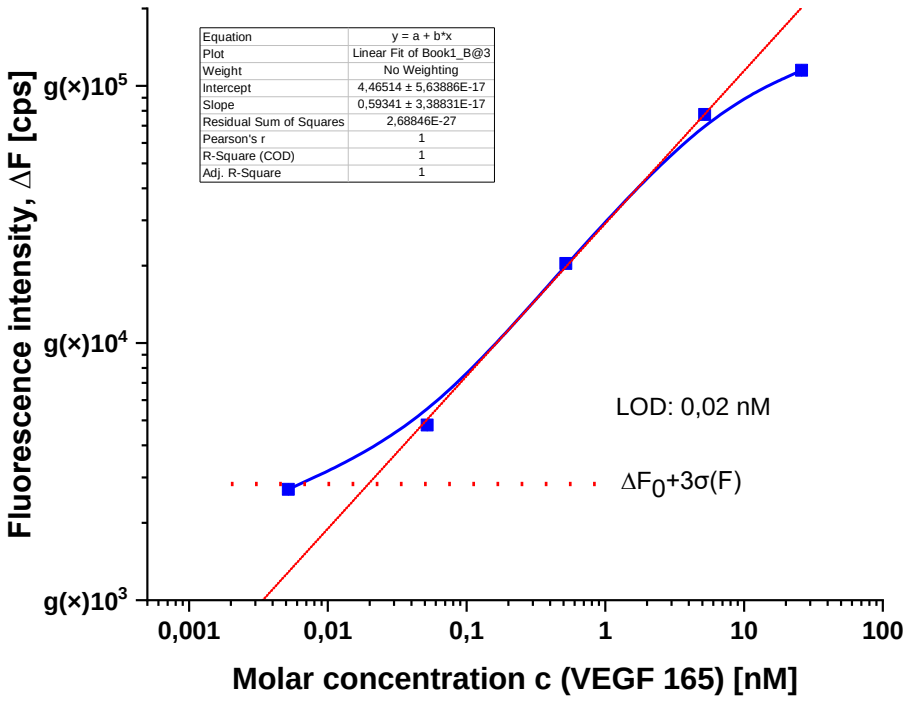

Figure 25: Calibration curve of VEGF 165.

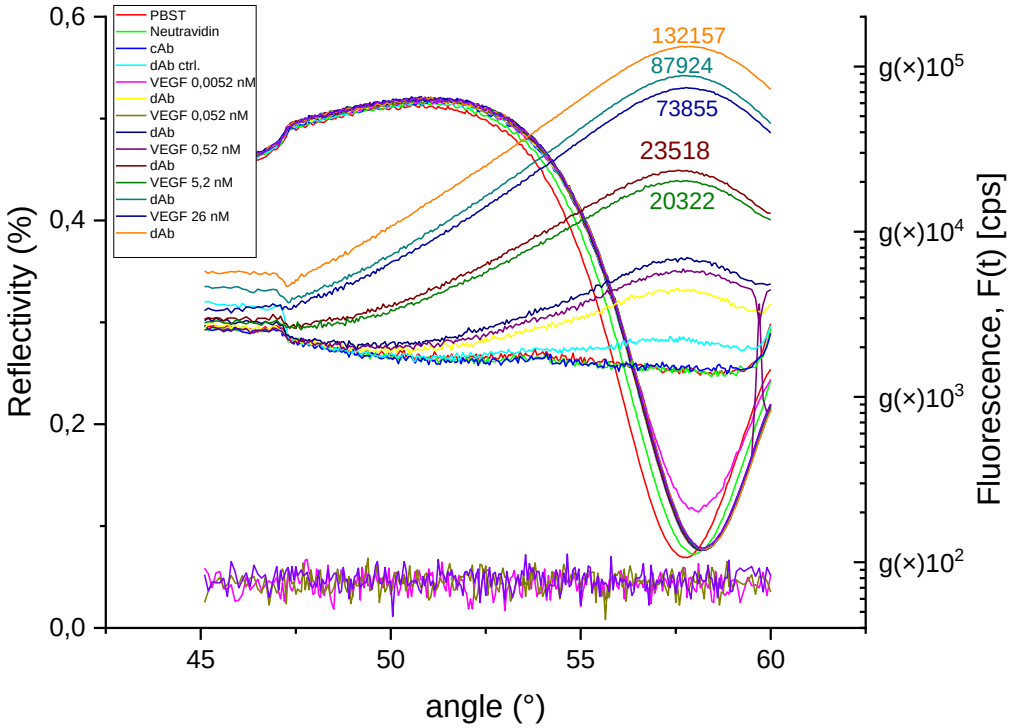

Figure 26: Angular reflectivity spectrum to determine the layer thickness of the metal surface. The red line represents the angle being necessary to fulfill SPR condition in case of PBST. After Neutravidin was applied the angle of the green line shows a significant shift compared to PBST. Moreover, after flowing the capture antibody over the cell, another shift within the angle occurred (blue line). Another noticeable shift is evident in the pink line, which corresponds to the VEGF with the lowest concentration.

Regeneration (Biotin SAM 1:5)			
	Trial 1	**Trial 2**	**Trial 3**
Chemical	**concentration**		
Neutravidin	1,86 µM	1,86 µM	1,86 µM
Biotin Anti-VEGF 165A antibody (cAb)	6,25 nM	6,25 nM	6,25 nM
VEGF165 human recombinant, expressed in E. coli (Fisher Scientific)	26 nM	26 nM	26 nM
Anti-VEGF Antibody, Alexa Fluor® 647 Conjugate from rabbit (dAb)	9 nM	54 nM	27 nM
Glycine/HCl pH=3	+	-	-
Glycine/HCl pH=2	-	+	-
100 mM NaOH	-	-	+

Table 15: Used chemicals and concentrations for the regeneration of the system.

To regenerate the system, three regeneration solutions were investigated to remove both the analyte and the detection antibody from the surface. Table 15 shows the chemicals, their concentrations as well as the different regeneration buffers used for the experiments.

At first, a glycine/HCl buffer with pH=3 was investigated regarding its ability to remove the applied analyte as well as dAb, as can be seen in Figure 27. Prior to applying the buffer, Neutravidin, cAb, analyte and dAb were immobilized onto the biotin SAM. The buffer was then applied for 2-3 minutes followed by PBST to observe the response signal. In total, the system was exposed to the buffer for 30 minutes until the SPR signal decreased to the baseline of the capture antibody at -0.17 mRIU. To check if Neutravidin as well as cAb still remained on the surface, the analyte and dAb were again applied. Since the signal showed an increase, it was concluded that VEGF was able to attach again on its corresponding capture antibody. The system underwent another 10-minute regeneration step, showing that it was again possible to remove analyte and detection antibody. However, the experiment was conducted within 2 days, which may have introduced potential sources of error: denaturation of the capture antibody, unspecific binding on the gold surface due to degradation of Neutravidin or the SAM or variation in temperature.

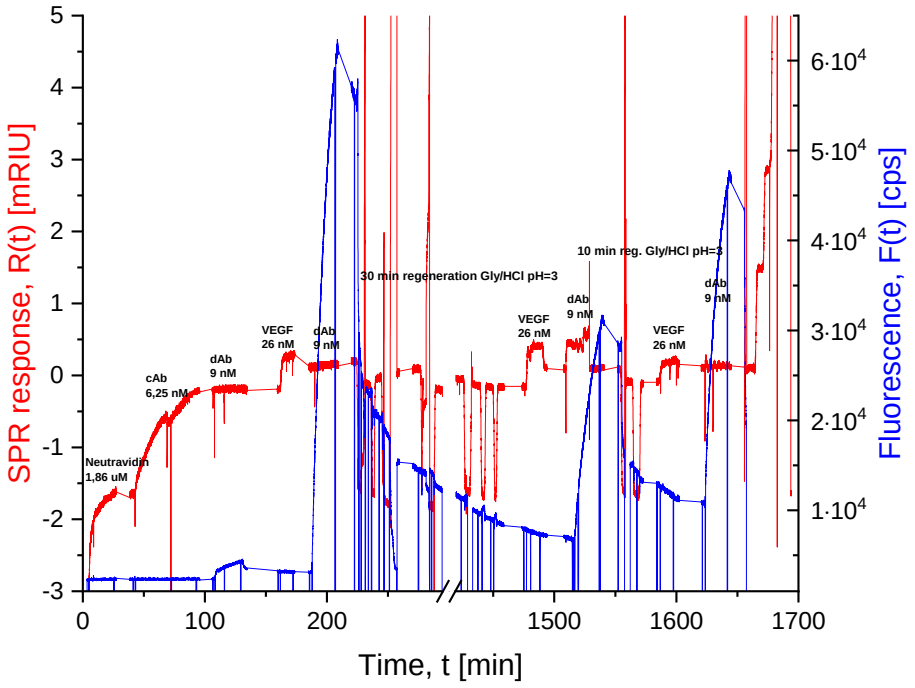

Figure 27: Regeneration of the system with the buffer Glycine/HCl pH=3.

The second buffer was glycine/HCl with pH=2. It was applied for 5 minutes, whereas it was checked in between to what extent the baseline increases again when flushing with PBST. The subsequent immobilization of VEGF led to an increase of the signal which was 5 times lower than the baseline observed before applying the regeneration buffer, *i.e.* 0.04 mRIU instead of 0.2 mRIU. For that reason, it had been concluded that the conditions of this buffer were too harsh to maintain the capacity the system prior had. Another evidence of this assumption is the fluorescence signal appearing after the application of dAb at 300 min. Compared to the prior fluorescence signal at 180 min its magnitude showed only half of the signal.

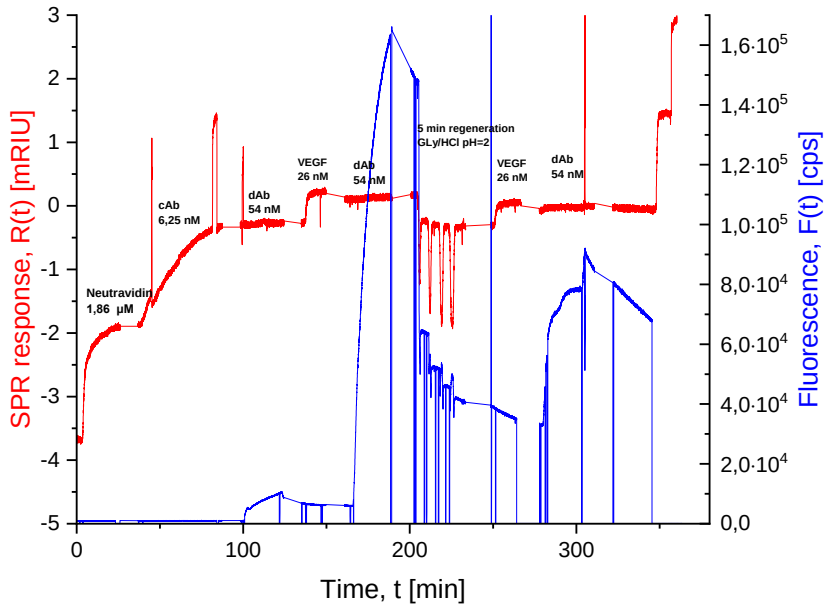

Figure 28: Regeneration of the system with the buffer Glycine/HCl pH=2.

The third solution investigated was 100 mM NaOH. The first regeneration step was done after 250 minutes. 100 mM NaOH was applied for 10 minutes, which can be seen in Figure 29. Even if the subsequent application of VEGF led to an increase in the SPR signal, its baseline was lower than the baseline of the capture antibody leading to the conclusion that this buffer was that harsh that it was able to detach the cAb to some extent. Moreover, after 275 min the dAb was applied. The corresponding fluorescence signal increased to an extent, which was in a similar range observed before introducing 100 mM NaOH. This might had occurred due to unspecific binding at the remaining cAb.

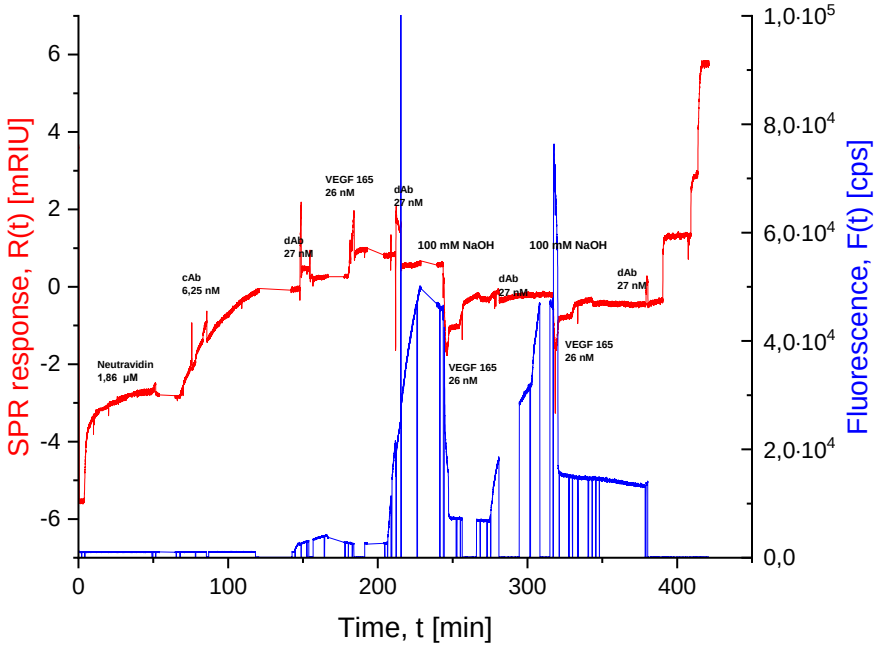

Figure 29: Regeneration of the system with 100 mM NaOH.

To summarize the results: the buffer Glycin/HCl at pH=3 performed best. Due to time constraints, the experiment could not be repeated. However, this needs to be done to ensure no errors occur.

Control with Interleukin-6 (Biotin SAM 1:5)	
Chemical	**concentration**
Neutravidin	1,86 µM
Biotin Anti-VEGF 165A antibody (cAb)	6,25 nM
IL-6	4,8 nM 24 nM
Anti-VEGF Antibody, Alexa Fluor® 647 Conjugate from rabbit (dAb)	54 nM

Table 16: Used chemicals and concentrations for the control with IL-6.

To ensure the selectivity of the capture antibody, a control experiment with Interleukin-6 was conducted. Figure 30 shows the corresponding SPR measurement. After the first application of IL-6 one could observe an increase in the SPR-signal. Nevertheless, the signal decreased to its prior state after washing with PBST, leading to the conclusion that IL-6 did not remain on the surface and thus did not increase the fluorescence signal notably after applying dAb. However, this figure reveals the extent of unspecific binding, since the fluorescence signal increased after applying dAb. Within the angular reflectivity spectrum, the fluorescence signal is illustrated in counts per seconds, showing that the addition of IL-6 did not cause a substantial increase of the signal. The red line corresponds to PBST, whereas the green line denotes the shift in the angle after applying Neutravidin. The blue line represents the signal obtained after applying cAb. For those the fluorescence signal did not increase at all. However, after alternating application of dAb and IL-6 an increase in the fluorescence signal is observed. The turquoise, yellow and dark blue line denote the signal after introducing dAb, whereas the pink and olive-green line represents IL-6.

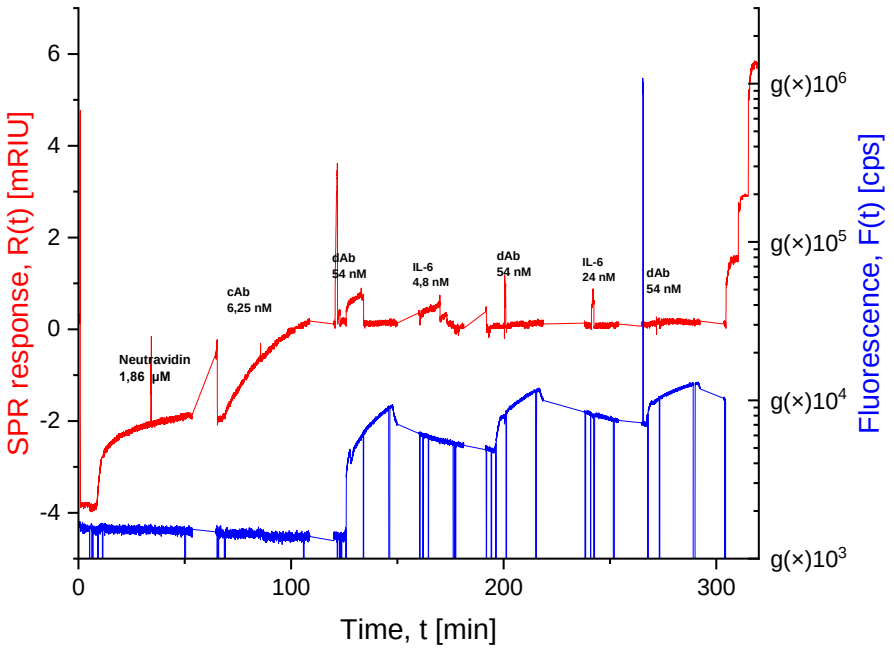

Figure 30: Control experiment with IL-6.

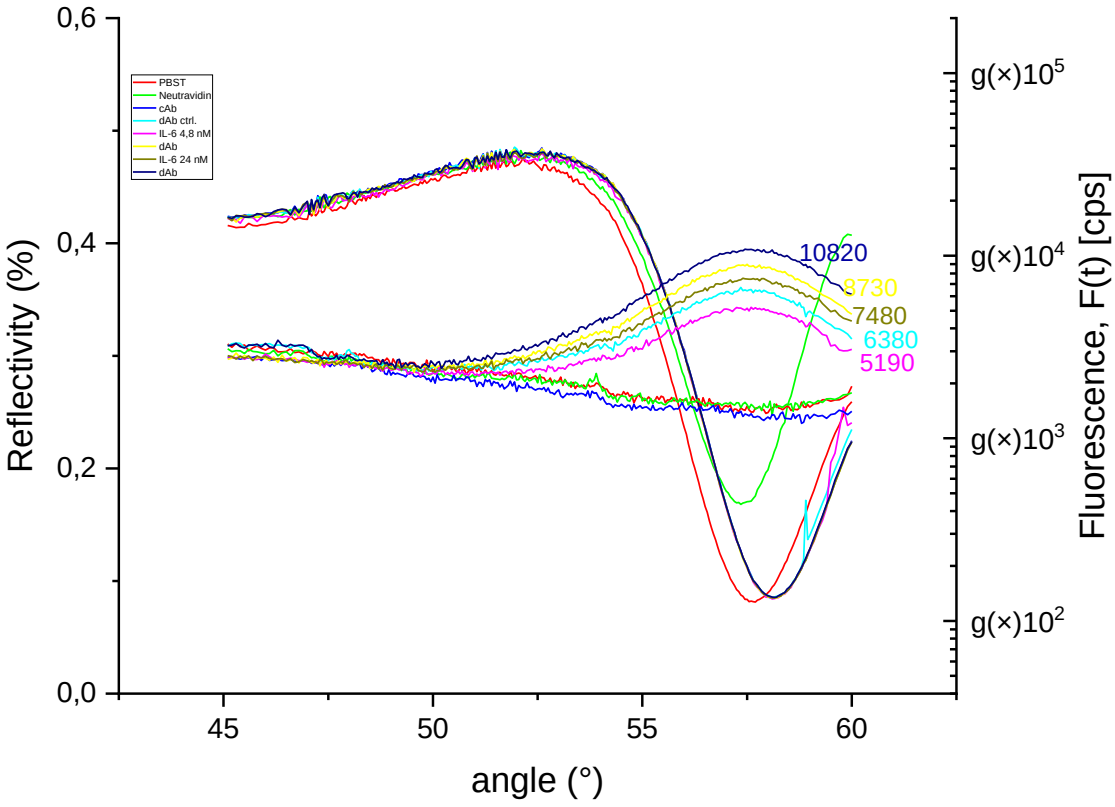

Figure 31: Angular reflectivity spectrum of the control experiment with IL-6.

Titration of 10% Serum spiked with VEGF-A (Biotin SAM 1:5)	
Chemical	**concentration**
Neutravidin	1,86 µM
Biotin Anti-VEGF 165A antibody (cAb)	6,25 nM
Human blood Serum	-
VEGF165 human recombinant, expressed in E. coli (Fisher Scientific)	0,0052 nM 0,052 nM 0,52 nM 5,2 nM 26 nM
Anti-VEGF Antibody, Alexa Fluor® 647 Conjugate from rabbit (dAb)	54 nM

Table 17: Used chemicals and concentrations for the titration of 10% serum spiked with VEGF-A.

To estimate the influence of serum, which contains both interfering molecules as well as naturally occurring VEGF, a titration of 10% serum spiked with VEGF-A was performed, as depicted in Figure 32. The higher the VEGF concentration, the higher the corresponding fluorescence signal. Compared to the titration shown in Figure 24 the serum does not seem to have a large influence on the result, since the fluorescence signal is in the same range. However, Figure 33 shows the corresponding angular reflectivity spectrum, indicating that the fluorescence signal was indeed higher for all applied

concentrations. The red line in the spectrum signifies PBST, while the green line represents the shift in the angle after Neutravidin application. The blue line corresponds to the signal obtained post cAb application, where fluorescence signal still remained unchanged. However, upon alternating application of dAb and sera-VEGF, a noticeable increase in fluorescence signal is observed. Thus, one can conclude that there are compounds present in sera-VEGF, which influence the signal. Moreover, the LOD was determined to 0.015 nM, as can be seen in Figure 34. However, this value results from measuring only at two concentrations, since serum spiked with VEGF saturated earlier compared to the titration of VEGF 165. Thus, it has to be taken with a grain of salt.

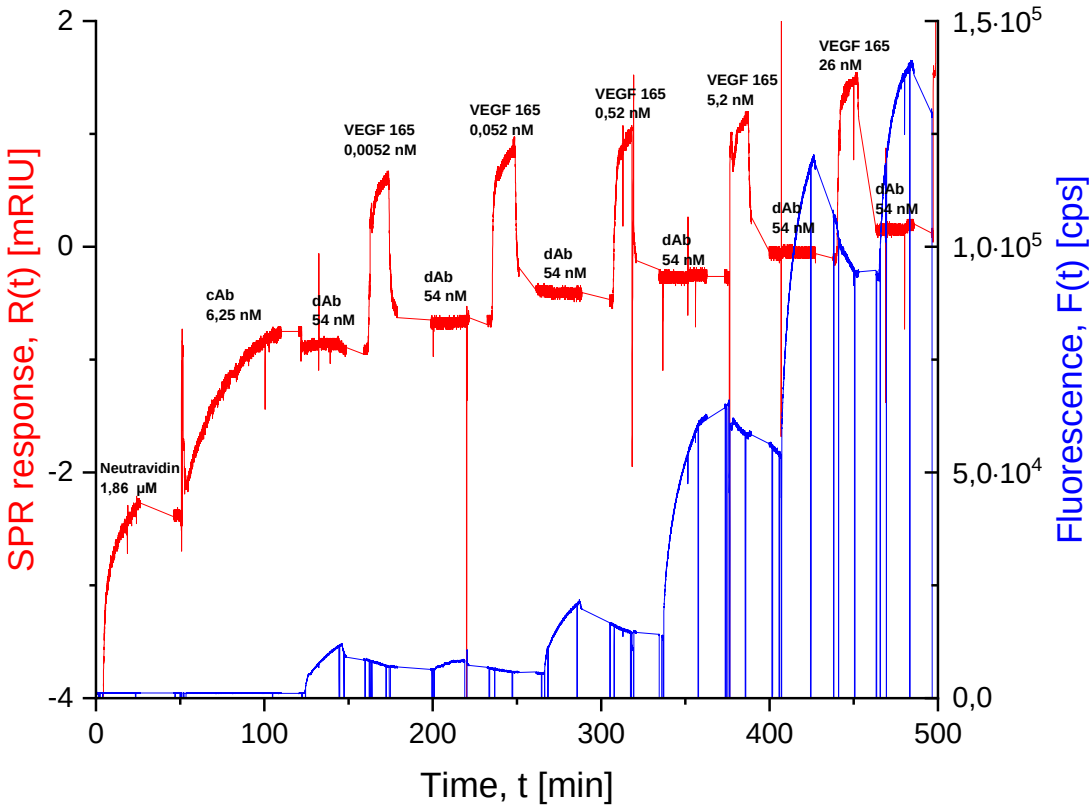

Figure 32: SPR measurement of the titration of 10 % serum spiked with VEGF-A.

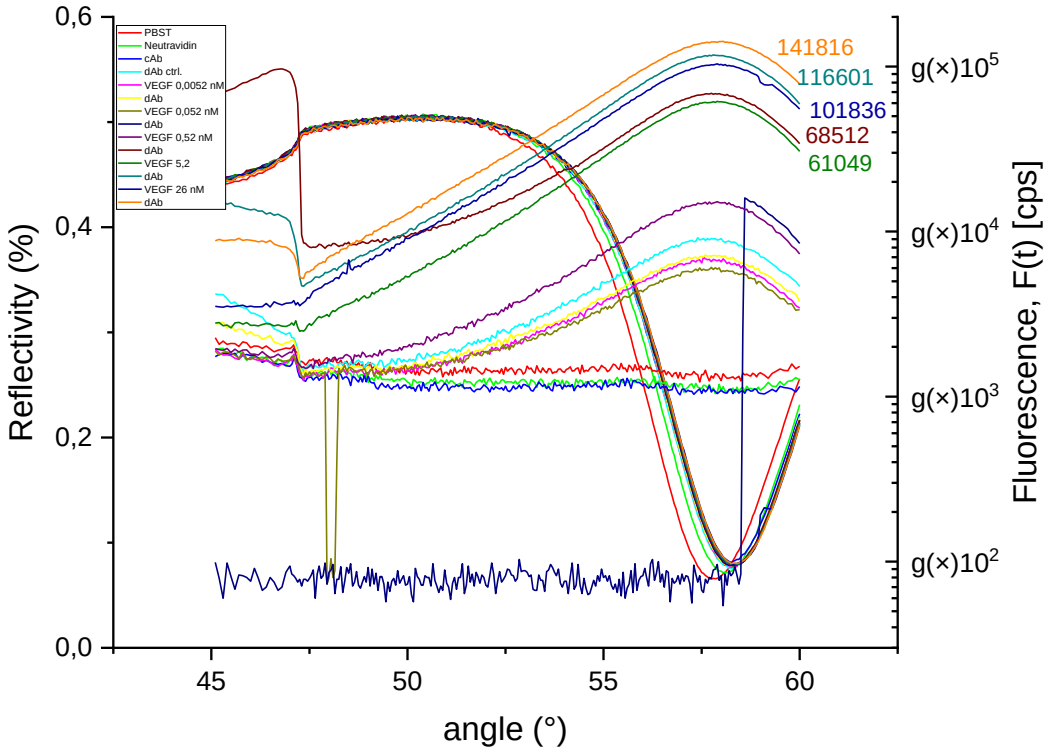

Figure 33: Angular reflectivity spectrum of the titration of 10% serum spiked with VEGF.

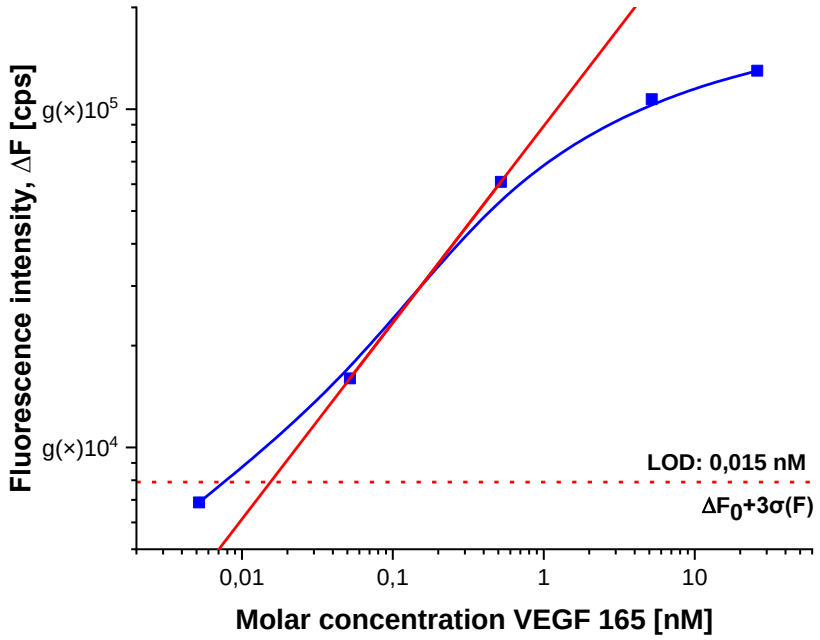

Figure 34: Calibration curve of 10% serum spiked with VEGF 165.

4.2 MIP-QCM approach

SEM

Scanning electron microscopy (SEM) served to take images of nanoMIPs-A high- and low affinity particles to measure their diameter. Figure 35 and Figure 36 depict the images obtained, showing that HA particles are smaller and have a narrower size distribution, than LA particles. Table 18 gives the corresponding diameter and standard deviation.

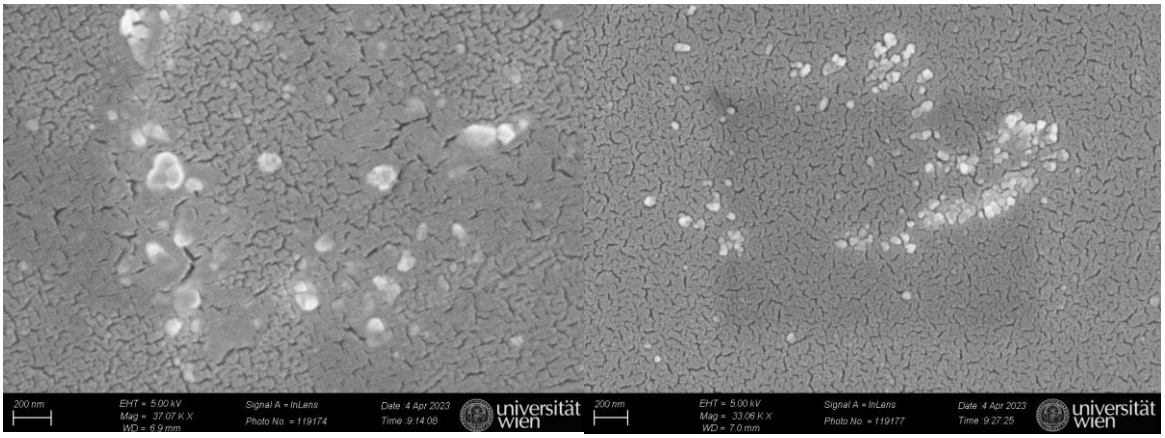

Figure 35: High affinity nanoMIP-A particles.

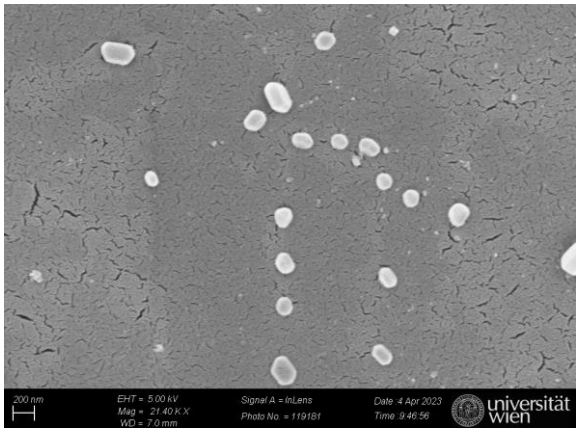

Figure 36: Low affinity nanoMIP-A particles.

	$\bar{X}$	**σ**
High affinity	69 nm	14 nm
Low affinity	195 nm	103 nm

Table 18: Average and standard deviation of high- and low affinity nanoMIP particles.

DLS

Figure 37 shows the number distribution of nanoMIP-A HA particles. With each measurement run, the peak shifts to a larger size, implying that the nanoparticle suspension is not stable; since they quickly aggregate, forming increasingly larger clusters. Compared to Figure 38, the nanoMIPs-B_HA seem to be more stable in solution since peaks do not shift between runs.

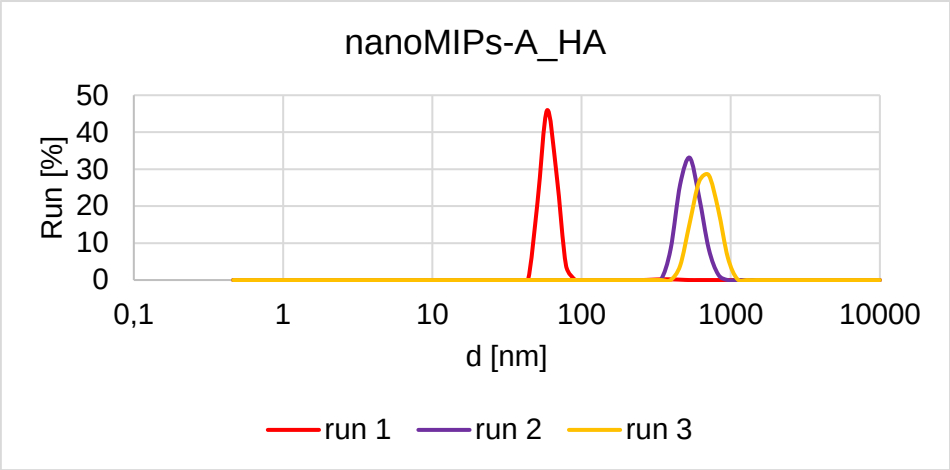

Figure 37: Number distribution of nanoMIPs-A_HA.

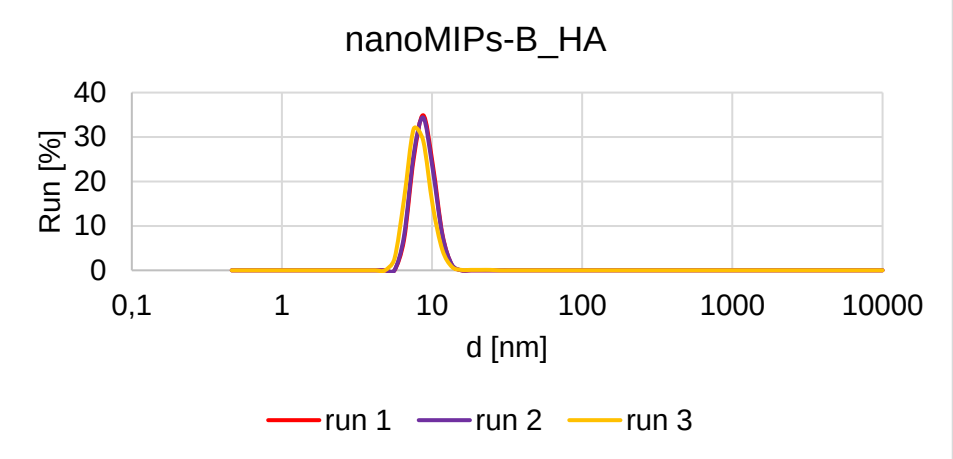

Figure 38: Number distribution of nanoMIPs-B_HA.

As can be seen in Table 19 and Table 20 the polydispersity index (PDI) of NanoMIPs-A_HA is larger than that of NanoMIPs-B_HA indicating that B has a narrower size distribution. However, the PDI is quite high (> 0.4) for both suggesting a relatively broad size distribution. This should be optimized in future synthesis. Moreover, B_HA is more strongly charged than A_HA, which is consistent with stability observations.

Run	PDI	Zeta Potential [mV]
1	0,79	-9,02
2	0,602	-7,93
3	0,463	-10
Average	0,6	-9
Stdev	0,16	1,04

Table 19: PDI and Zeta Potential for NanoMIPs-A_HA.

Run	PDI	Zeta Potential [mV]
1	0,443	-12
2	0,398	-16,1
3	0,679	-21,1
Average	0,5	-16,4
Stdev	0,15	4,56

Table 20: PDI and Zeta Potential for NanoMIPs-B_HA.

QCM measurements

In a first step, the conjugation of the VEGF epitope to Glutaraldehyde was investigated via QCM measurement. For that purpose, one QCM was incubated with Glutaraldehyde and another QCM was incubated with Ethanolamine- as a blocking agent. Figure 39 and Figure 40 show the data obtained from a simultaneous measurement after injecting the epitope and nanoMIPs-A_HA. The red lines correspond to the frequency signals of QCMs which were incubated with ethanolamine, whereas the black ones show the QCMs which only underwent glutaraldehyde incubation. As can be seen in both figures, the frequency of the ethanolamine-incubated QCMs did not decrease much after injecting 500 ppm of the epitope, whereas the frequency of the Glutaraldehyde-incubated QCMs do. In Figure 39 the decrease in frequency is about 100 Hz for the Glutaraldehyde incubated QCM, whereas in Figure 40 the decrease is about 140 Hz. This leads to the conclusion that the desired reaction between Glutaraldehyde and VEGF epitope had taken place. Moreover, it was investigated in both experiments, if the conjugated VEGF epitope does bind 500 ppm of its nanoMIPs-A_HA. The cysteamine:butanethiol (Cys:Bu) mixture within this experiment was 1:6000. After injecting the nanoMIPs there was no significant decrease in the frequency leading to the insight that either the recipe of the polymerization mixture A had to be adapted to enable desired binding or that the concentration of the nanoMIPs needs increasing.

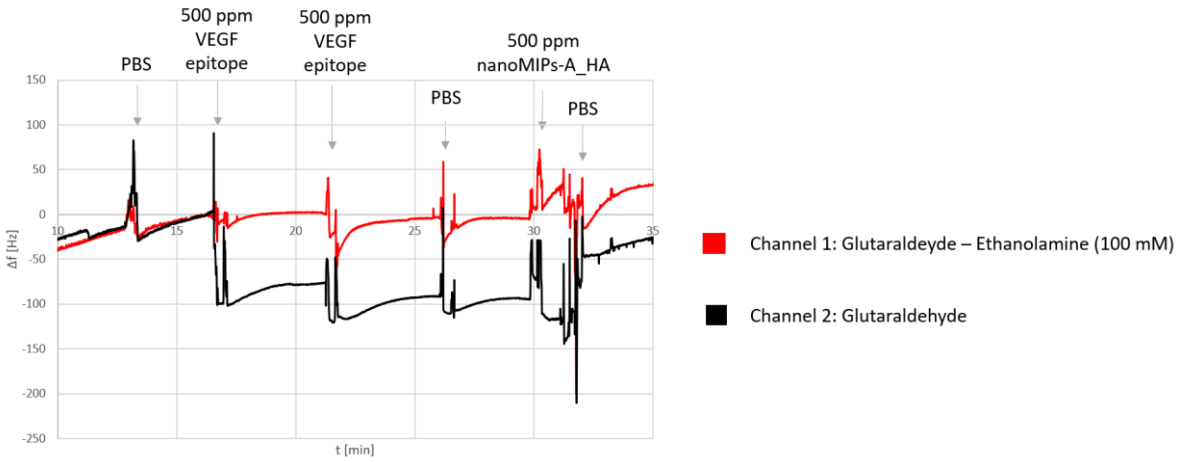

Figure 39: QCM measurement of the binding of Glutaraldehyde to VEGF and subsequent to its nanoMIPs-A_HA (black line) and the similar, simultaneous measurement of a QCM which was incubated with the blocking agent Ethanolamine (red line).

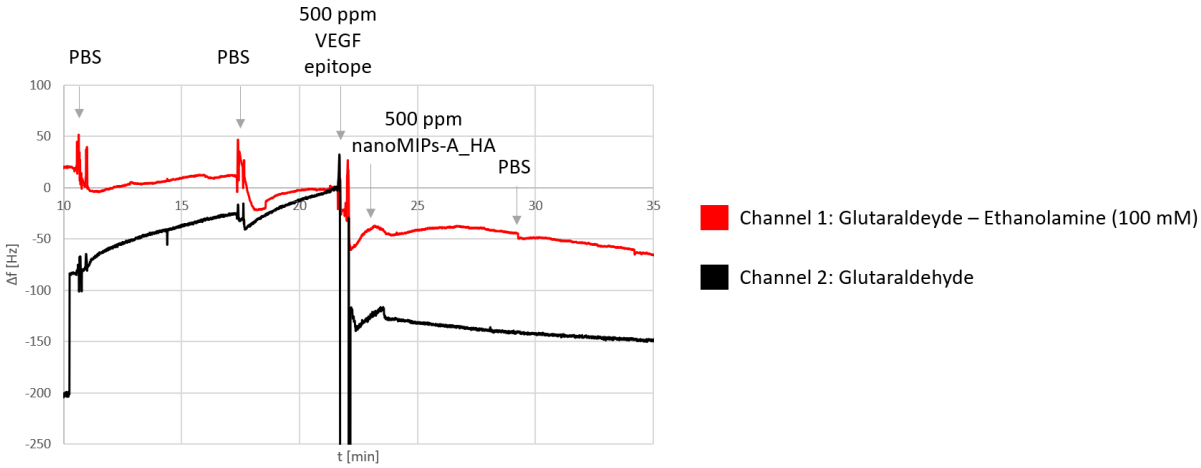

Figure 40: QCM measurement of the binding of Glutaraldehyde to VEGF and subsequent to its nanoMIPs-A_HA (black line) and the similar, simultaneous measurement of a QCM which was incubated with the blocking agent Ethanolamine (red line).

After increasing the concentration of the nanoMIPs-A_HA from 500 ppm to 2000 ppm, a significant decrease within the frequency of about 900 Hz was observed as depicted in Figure 41. The red line of channel 1 represents the QCM being incubated with VEGF epitope whereas the black line represents the QCM being incubated with ethanolamine. The Cys:Bu mixture within this experiment was 1:10 000.

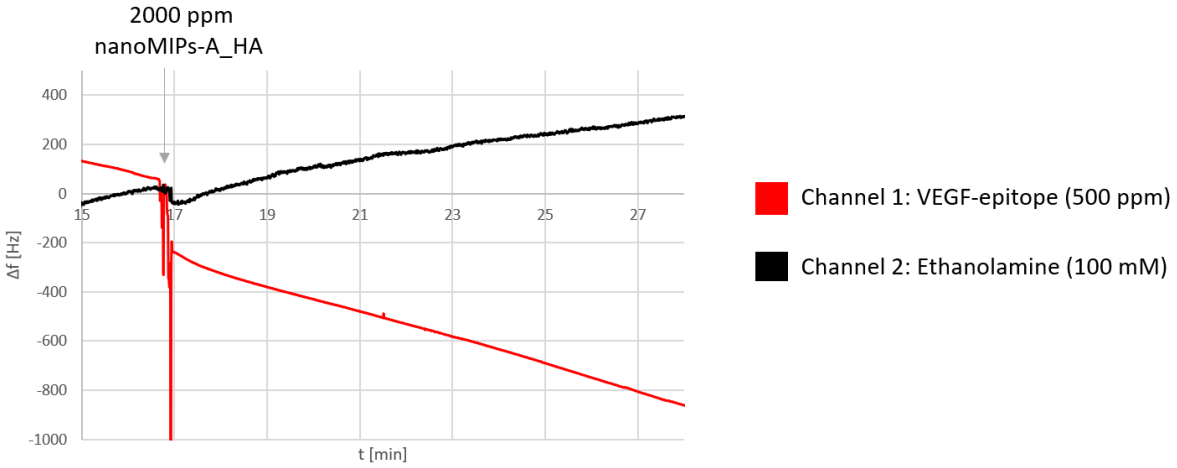

Figure 41: QCM measurement after injection of 2000 ppm of nanoMIPs-A_HA. Channel 1 (red line) shows the QCM which was incubated with VEGF and Channel 2 (black line) displays the frequency of the QCM which was previously incubated with ethanolamine.

It was further investigated if the nanoMIPs-A_HA bind to VEGF epitope sufficiently tightly to withstand washing with PBS. Figure 42 reveals that the binding from VEGF epitope to nanoMIPs-A_HA was indeed weak: one can use PBS to remove it. This clearly indicates that rather than changing the concentration of the nanoMIPs one needs to optimize the recipe of the polymerization mixture. The Cys:Bu mixture within this experiment was 1:560.

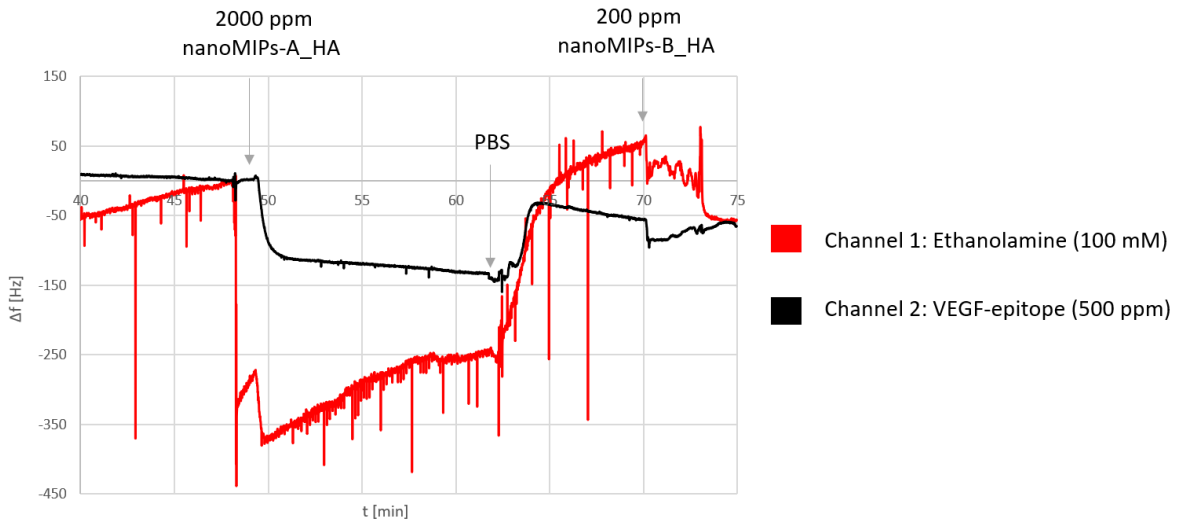

Figure 42: The frequency of the black line represents the QCM which was previously incubated with VEGF. It shows a decrease after the injection of nanoMIPs-A_HA but right after the injection of PBS it increases again, indicating the weak binding.

The Cys:Bu mixture within the following two experiments was 1:6000. The QCM was incubated with human serum albumin (HSA) instead of ethanolamine. The reason for this is that it occurs in blood serum, so one can estimate the extent to which it binds to MIPs. As can be seen in Figure 43, injecting 100 ppm nanoMIPs-B_HA led to a decrease of about 25 Hz of the frequency in channel 1 as well as in channel 2, leading to the insight that MIPs do also bind to HSA. However, only after injection of the undiluted nanoMIPs-B_HA solution a significant difference in the frequency was observed. For channel 1 the decrease was about 100 Hz, whereas for channel 2 it was about 50 Hz. Moreover, the MIPs remain on the QCMs after washing with MQ H_2O.

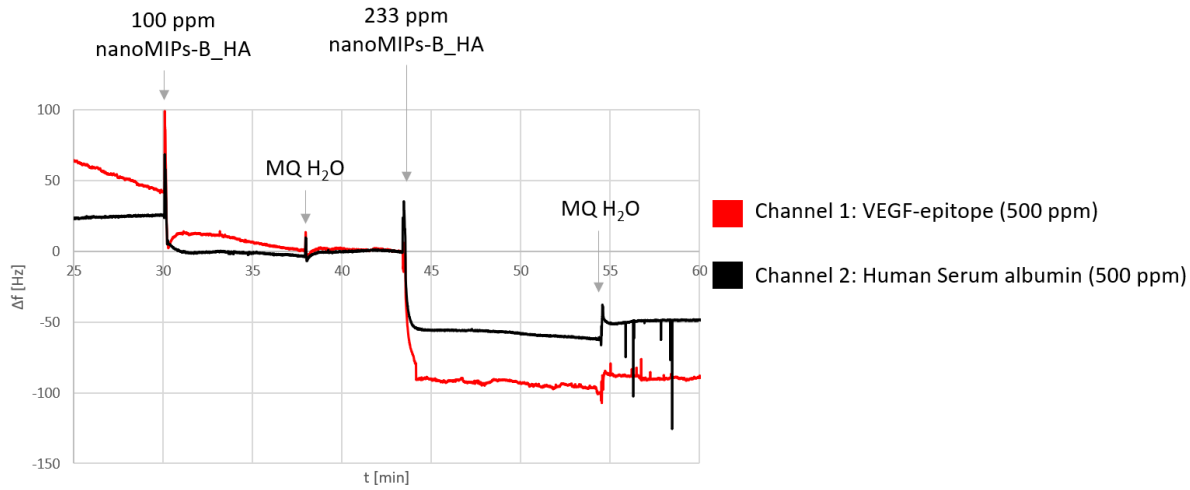

Figure 43: Channel 1 was incubated with VEGF, whereas channel 2 was incubated with HSA. In both cases a solution of 100 ppm of nanoMIPs-B_HA showed a slightly decrease in the frequency. Only after the addition of the undiluted nanoMIPs-B_HA a significant shift is observed. Washing with MQ H_2O didn't remove the nanoMIPs.

It has also been investigated if adding nanoMIPs-B_HA prior to nanoMIPs-A_HA has any influence on frequency. Indeed, the frequency decreases slightly, as can be seen in Figure 44. For channel 1, which was incubated with VEGF-epitope it decreased for about 100 Hz and for channel 2, which was incubated with HSA, for about 220 Hz.

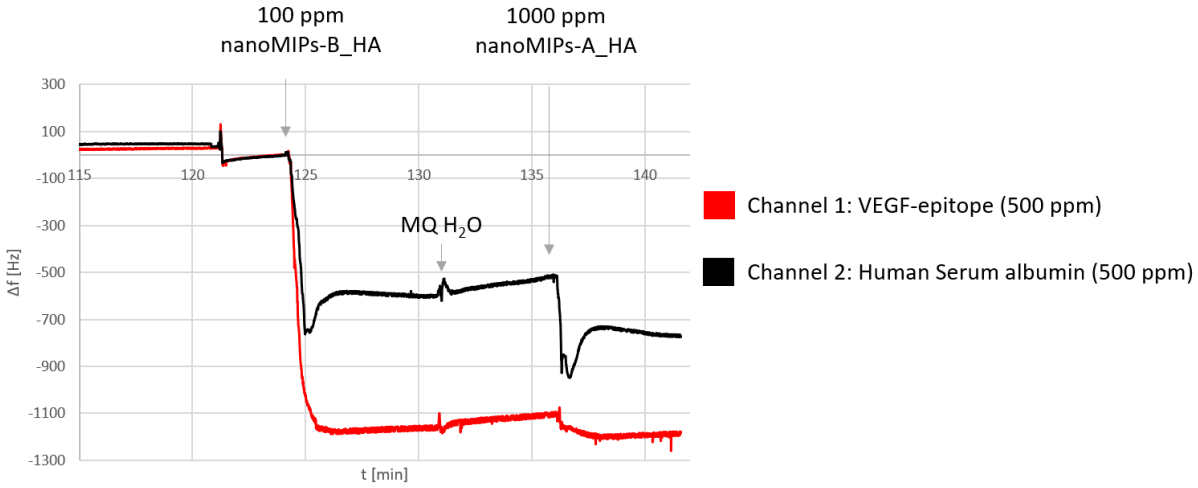

Figure 44: Channel 1 was incubated with VEGF and channel 2 was incubated with HSA. Addition of nanoMIPs-B_HA led to a decrease within the frequency. After washing with MQ H_2O the nanoMIPs remained attached.

Within the following two experiments the Cys:Bu mixture was 1:10 000. Channel 1 was incubated with VEGF epitope and channel 2 with HSA. After adding 116 ppm nanoMIPs-B_HA followed by 233 ppm nanoMIPs-B_HA, one can observe a significant decrease of the frequency, as can be seen in Figure 45. For channel 1 the frequency decreased in total by approximately 80 Hz and for channel 2 by 50 Hz. Figure 46 only shows one channel which was incubated with VEGF epitope prior to measuring. Repeated addition of 233 ppm nanoMIPs-B_HA leads to a frequency decrease by approximately 60 Hz. Nevertheless, adding MQ H_2O after 40 min and 57 min removes a small portion of the nanoMIPs.

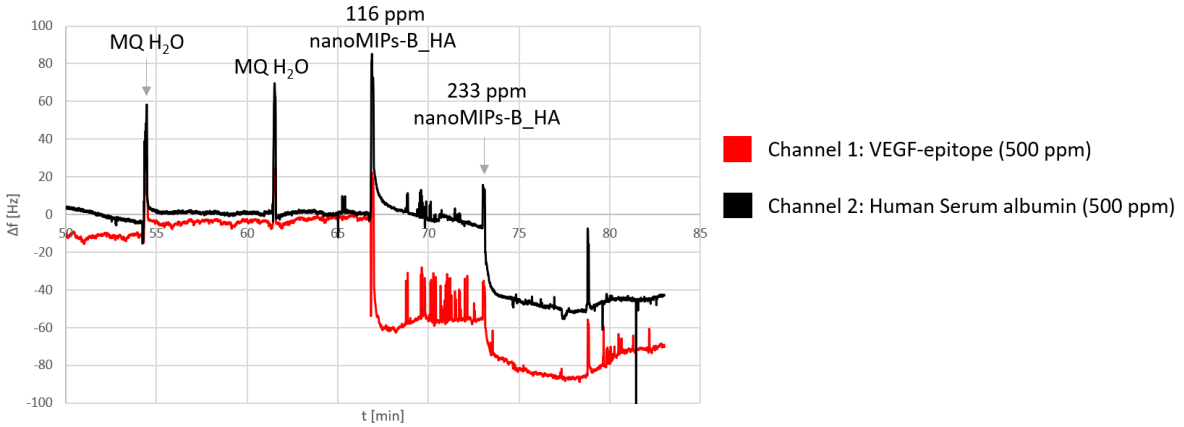

Figure 45: Channel 1 was prior incubated with VEGF and channel 2 with HSA. Addition of 233 ppm nanoMIPs-B_HA showed a significant decrease within the frequency.

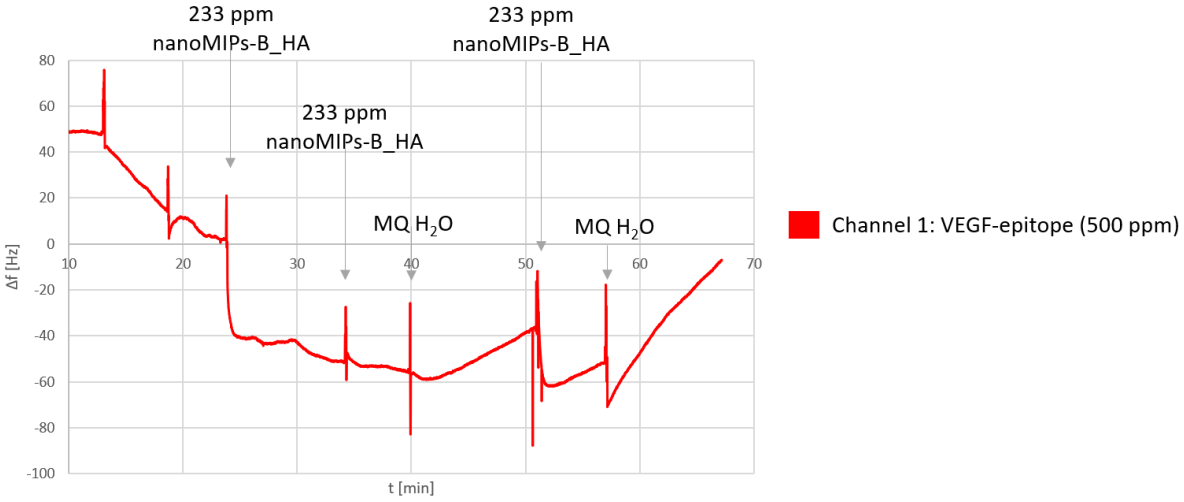

Figure 46: Channel 1 was incubated with VEGF. NanoMIPs-B_HA bind to its template leading to a decrease in frequency. MQ H_2O slightly removes the nanoMIPs as can be seen after its addition making the frequency to increase.

Overall, the experiments demonstrate binding between the VEGF template and nanoMIPs, although at the same time, there is non-specific binding to HSA, albeit to a lesser extent. It appears that the B particles, in terms of binding strength and size distribution seem to be the more promising recipe.

5. Summary and Outlook

Starting from assessing the optimal dAb concentration, which turned out 18 nM, titration yielded an LOD of 384 pg/mL (20pM) and is therefore clinically relevant. To regenerate the system, 3 regeneration solutions, glycine/HCl buffer pH=3, glycine/HCl buffer pH=2 and 100mM NaOH were investigated. Among those Glycine/HCl buffer pH=3 turned out to perform best. The selectivity of the system was tested by conducting a control experiment with IL-6. It has been shown that the capture antibody does not show any affinity towards this protein. Moreover, serum spiked with VEGF was tested to check its influence on the system. The data obtained show an increase within the fluorescence signal compared to the data without serum, indicating that the amount of serum compounds that attach to the surface greatly influence the signal. Within this experiment the LOD was determined as 15 pM, which is of clinical interest.

Based on the recipe from Canfarotta *et al*. two different polymerization mixtures were tested regarding their performance to establish nanoMIPs that are able to bind their target epitope sequence VEGF. The mixtures differ by using TBAM as a monomer, or not. It could be shown that polymers without TBAM lead to stronger binding, since it was not completely possible to remove the corresponding nanoMIPs by washing. The higher the concentration of nanoMIPs (100ppm – 233 ppm), the more the frequency decreased, leading to the insight, the amount of mass bound depends on sample concentration. A control experiment was performed to check the influence of HSA, an abundant protein occurring within blood. Indeed, some unspecific binding of HSA to the synthesized MIPs was observed, however to only half of the moiety than to the analyte. Moreover, three different functionalization mixtures were tested regarding their influence on binding to VEGF epitope. The Cys:Bu mixture with a ratio of 1:560 led to a poor decrease in the frequency, by approximately 30 Hz, when nanoMIPs-B_HA with a concentration of 200 ppm were applied. Most probably these poor interactions result from steric hindrance. Cys:Bu mixture with the ratio of 1:6000 led to stronger binding, since the frequency decreased to a higher extent of about 100 Hz. The ratio 1:10000 showed a frequency decrease in a similar range. However, more experiments are necessary to make accurate statements and to determine the linear range.

In general, the use of MIPs instead of antibodies promises great potential in biosensing approaches, since they are less prone to degradation due to their chemical structure. Moreover, they are more resistant when being exposed to harsh conditions such as alterations in pH and temperature. To determine the LOD of VEGF via the ELISA-SPR approach concentrations of 0.0052 nM – 26 nM were used. Compared to the MIPs-QCM approach the VEGF epitope being used had a concentration of 347 mM. Thus, the implementation of MIPs in a SPR system offers advantages: the SPR system provides higher sensitivity, whereas the MIPs are more resistant to harsh conditions.

Overall, the goal to develop two systems, one via ELISA-SPR and the other via MIPs-QCM, to detect VEGF was successfully reached. Future experiments will need to optimize parameters such as suppression of unspecific interactions as well as adaption of the polymerization mixture to achieve narrower size distribution of particles.

6. Appendix

Abstract

VEGF is a signaling protein that plays a key role in the formation of new blood vessels by supplying them with nutrients and oxygen. Thus, it is necessary for normal development as well as for wound healing. Nevertheless, it plays a role in various pathological conditions, particularly cancer, where the abnormal formation of blood vessels is a characteristic feature of tumor development. For that reason, monitoring the VEGF level within the blood stream is of great interest, since this gives information about health status.

This thesis focusses on the development of two sensors for detecting VEGF. One of them uses an Enzyme Linked Immunosorbent Assay (ELISA), which was optimized and implemented on a system using surface plasmon resonance (SPR). The second uses molecularly imprinted polymers (MIPs), which had been tailor made synthesized towards a particular VEGF epitope sequence, to provide a robust alternative to antibodies – their natural counterparts. The compatibility between the MIPs and the VEGF epitope was tested via a mass-sensitive quartz crystal microbalance.

For future perspectives MIPs can also be implemented in the SPR system to avoid the use of sensitive and costly antibodies.

Kurzfassung

Vascular Endothelial Growth Facor ist ein Signalprotein, das eine entscheidende Rolle bei der Bildung neuer Blutgefäße spielt, indem es ihnen die Versorgung mit Nährstoffen und Sauerstoff ermöglicht. Daher ist es für die normale Entwicklung sowie für die Wundheilung unerlässlich. Dennoch ist es an verschiedenen pathologischen Zuständen, insbesondere bei Krebs, beteiligt, wo die abnormale Bildung von Blutgefäßen ein charakteristisches Merkmal der Tumorentwicklung ist. Aus diesem Grund ist die Überwachung des VEGF-Spiegels im Blut von großem Interesse, da dies Informationen über den Gesundheitszustand liefern kann.

Diese Arbeit konzentriert sich auf die Entwicklung von zwei Biosensoren zur Detektion von VEGF. Einer von ihnen verwendet einen Enzyme Linked Immunosorbent Assay (ELISA), der optimiert und in ein System mit Oberflächenplasmonenresonanz (SPR) implementiert wurde. Der zweite verwendet molekular geprägte Polymere (MIPs), die maßgeschneidert auf eine bestimmte VEGF-Sequenz synthetisiert wurden, um eine robuste Alternative zu Antikörpern - ihren natürlichen Gegenstücken - bereitzustellen. Mit einer massensensitiven Quarzkristallmikrowaage (QCM) wurde ihre Kompatibilität getestet.

Für die Zukunft ist es erstrebenswert MIPs auch in ein SPR-System zu implementieren, um den Einsatz empfindlicher und kostspieliger Antikörper zu vermeiden.

List of figures

List of equations

List of tables

References

(1) Betsholtz, C. Cell–Cell Signaling in Blood Vessel Development and Function. *EMBO Mol. Med.* **2018**, *10* (3). https://doi.org/10.15252/emmm.201708610.

(2) Joussen, A. M.; Kirchhof, B.; Gottstein, C. Molekulare Mechanismen Der Vaskulogenese Und Angiogenese. *Ophthalmol.* **2003**, *100* (4), 284–291. https://doi.org/10.1007/s00347-003-0799-x.

(3) Woolard, J.; Bevan, H. S.; Harper, S. J.; Bates, D. O. Molecular Diversity of VEGF-A as a Regulator of Its Biological Activity. *Microcirculation* **2009**, *16* (7), 572–592. https://doi.org/10.1080/10739680902997333.

(4) Ferrara, N. Role of Vascular Endothelial Growth Factor in Physiologic and Pathologic Angiogenesis: Therapeutic Implications. *Semin. Oncol.* **2002**, *29* (6Q), 10–14. https://doi.org/10.1053/sonc.2002.37264.

(5) Celletti, F. L.; Waugh, J. M.; Amabile, P. G.; Brendolan, A.; Hilfiker, P. R.; Dake, M. D. Vascular Endothelial Growth Factor Enhances Atherosclerotic Plaque Progression. *Nat. Med.* **2001**, *7* (4), 425–429. https://doi.org/10.1038/86490.

(6) Caldwell, R. B.; Bartoli, M.; Behzadian, M. A.; El-Remessy, A. E. B.; Al-Shabrawey, M.; Platt, D. H.; Caldwell, R. W. Vascular Endothelial Growth Factor and Diabetic Retinopathy: Pathophysiological Mechanisms and Treatment Perspectives. *Diabetes Metab. Res. Rev.* **2003**, *19* (6), 442–455. https://doi.org/10.1002/dmrr.415.

(7) Adamis, A. P.; Miller, J. W.; Bernal, M.-T.; D'Amico, D. J.; Folkman, J.; Yeo, T.-K.; Yeo, K.-T. Increased Vascular Endothelial Growth Factor Levels in the Vitreous of Eyes With Proliferative Diabetic Retinopathy. *Am. J. Ophthalmol.* **1994**, *118* (4), 445–450. https://doi.org/10.1016/S0002-9394(14)75794-0.

(8) Brockington, A.; Lewis, C.; Wharton, S.; Shaw, P. J. Vascular Endothelial Growth Factor and the Nervous System: VEGF and the Nervous System. *Neuropathol. Appl. Neurobiol.* **2004**, *30* (5), 427–446. https://doi.org/10.1111/j.1365-2990.2004.00600.x.

(9) Luttun, A.; Autiero, M.; Tjwa, M.; Carmeliet, P. Genetic Dissection of Tumor Angiogenesis: Are PlGF and VEGFR-1 Novel Anti-Cancer Targets? *Biochim. Biophys. Acta BBA - Rev. Cancer* **2004**, *1654* (1), 79–94. https://doi.org/10.1016/j.bbcan.2003.09.002.

(10) Cébe Suarez, S.; Pieren, M.; Cariolato, L.; Arn, S.; Hoffmann, U.; Bogucki, A.; Manlius, C.; Wood, J.; Ballmer-Hofer, K. A VEGF-A Splice Variant Defective for Heparan Sulfate and Neuropilin-1 Binding Shows Attenuated Signaling through VEGFR-2. *Cell. Mol. Life Sci.* **2006**, *63* (17), 2067–2077. https://doi.org/10.1007/s00018-006-6254-9.

(11) Del Gaudio, F.; Liu, D.; Lendahl, U. Notch Signalling in Healthy and Diseased Vasculature. *Open Biol.* **2022**, *12* (4), 220004. https://doi.org/10.1098/rsob.220004.

(12) Canfarotta, F.; Poma, A.; Guerreiro, A.; Piletsky, S. Solid-Phase Synthesis of Molecularly Imprinted Nanoparticles. *Nat. Protoc.* **2016**, *11* (3), 443–455. https://doi.org/10.1038/nprot.2016.030.

(13) Neufeld, G.; Cohen, T.; Gengrinovitch, S.; Poltorak, Z. Vascular Endothelial Growth Factor (VEGF) and Its Receptors. *FASEB J.* **1999**, *13* (1), 9–22. https://doi.org/10.1096/fasebj.13.1.9.

(14) Shibuya, M. Vascular Endothelial Growth Factor (VEGF) and Its Receptor (VEGFR) Signaling in Angiogenesis: A Crucial Target for Anti- and Pro-Angiogenic Therapies. *Genes Cancer* **2011**, *2* (12), 1097–1105. https://doi.org/10.1177/1947601911423031.

(15) Park, S. A.; Jeong, M. S.; Ha, K.-T.; Jang, S. B. Structure and Function of Vascular Endothelial Growth Factor and Its Receptor System. *BMB Rep.* **2018**, *51* (2), 73–78. https://doi.org/10.5483/BMBRep.2018.51.2.233.

(16) Dvorak, H. F. Vascular Permeability Factor/Vascular Endothelial Growth Factor: A Critical Cytokine in Tumor Angiogenesis and a Potential Target for Diagnosis and Therapy. *J. Clin. Oncol.* **2002**, *20* (21), 4368–4380. https://doi.org/10.1200/JCO.2002.10.088.

(17) Yamamoto, Y.; Toi, M.; Kondo, S.; Matsumoto, T.; Suzuki, H.; Kitamura, M.; Tsuruta, K.; Taniguchi, T.; Okamoto, A.; Mori, T.; Yoshida, M.; Ikeda, T.; Tominaga, T. Concentrations of Vascular Endothelial Growth Factor in the Sera of Normal Controls and Cancer Patients. *Clin. Cancer Res. Off. J. Am. Assoc. Cancer Res.* **1996**, *2* (5), 821–826.

(18) Prasad, P. N. *Introduction to Biophotonics*; John Wiley & Sons, Inc.: Hoboken, NJ, USA, 2003. https://doi.org/10.1002/0471465380.

(19) Pandule, S. S. Organic Receptors for Chemical Sensors Realized on Flexible Substrates; 2014.

(20) Yüce, M.; Kurt, H. How to Make Nanobiosensors: Surface Modification and Characterisation of Nanomaterials for Biosensing Applications. *RSC Adv* **2017**, *7* (78), 49386–49403. https://doi.org/10.1039/C7RA10479K.

(21) Ferreira, M. D. P.; Yamada-Ogatta, S. F.; Teixeira Tarley, C. R. Electrochemical and Bioelectrochemical Sensing Platforms for Diagnostics of COVID-19. *Biosensors* **2023**, *13* (3), 336. https://doi.org/10.3390/bios13030336.

(22) *Surface Plasmon Resonance Based Sensors*; Homola, J., Ed.; Springer Series on Chemical Sensors and Biosensors; Springer Berlin Heidelberg: Berlin, Heidelberg, 2006; Vol. 4. https://doi.org/10.1007/b100321.

(23) Jain, A.; Barve, A.; Zhao, Z.; Jin, W.; Cheng, K. Comparison of Avidin, Neutravidin, and Streptavidin as Nanocarriers for Efficient siRNA Delivery. *Mol. Pharm.* **2017**, *14* (5), 1517–1527. https://doi.org/10.1021/acs.molpharmaceut.6b00933.

(24) Sut, T. N.; Park, H.; Koo, D. J.; Yoon, B. K.; Jackman, J. A. Distinct Binding Properties of Neutravidin and Streptavidin Proteins to Biotinylated Supported Lipid Bilayers: Implications for Sensor Functionalization. *Sensors* **2022**, *22* (14), 5185. https://doi.org/10.3390/s22145185.

(25) Popov, P. LIQUID CRYSTAL INTERFACES: EXPERIMENTS, SIMULATIONS AND BIOSENSORS. **2015**. https://doi.org/10.13140/RG.2.2.34587.46883.

(26) Pasquardini, L.; Bossi, A. M. Molecularly Imprinted Polymers by Epitope Imprinting: A Journey from Molecular Interactions to the Available Bioinformatics Resources to Scout for Epitope Templates. *Anal. Bioanal. Chem.* **2021**, *413* (24), 6101–6115. https://doi.org/10.1007/s00216-021-03409-1.

(27) Kadhem, A. J.; Gentile, G. J.; Fidalgo de Cortalezzi, M. M. Molecularly Imprinted Polymers (MIPs) in Sensors for Environmental and Biomedical Applications: A Review. *Molecules* **2021**, *26* (20), 6233. https://doi.org/10.3390/molecules26206233.

(28) Kastritis, P. L.; Bonvin, A. M. J. J. On the Binding Affinity of Macromolecular Interactions: Daring to Ask Why Proteins Interact. *J. R. Soc. Interface* **2013**, *10* (79), 20120835. https://doi.org/10.1098/rsif.2012.0835.

(29) Chen, J.; Sawyer, N.; Regan, L. Protein-Protein Interactions: General Trends in the Relationship between Binding Affinity and Interfacial Buried Surface Area: Protein-Protein Interactions. *Protein Sci.* **2013**, *22* (4), 510–515. https://doi.org/10.1002/pro.2230.

(30) Yang, K.; Li, S.; Liu, L.; Chen, Y.; Zhou, W.; Pei, J.; Liang, Z.; Zhang, L.; Zhang, Y. Epitope Imprinting Technology: Progress, Applications, and Perspectives toward Artificial Antibodies. *Adv. Mater.* **2019**, *31* (50), 1902048. https://doi.org/10.1002/adma.201902048.

(31) Titirici, M. M.; Hall, A. J.; Sellergren, B. Hierarchical Imprinting Using Crude Solid Phase Peptide Synthesis Products as Templates. *Chem. Mater.* **2003**, *15* (4), 822–824. https://doi.org/10.1021/cm025770j.

(32) Muller, Y. A.; Christinger, H. W.; Keyt, B. A.; de Vos, A. M. The Crystal Structure of Vascular Endothelial Growth Factor (VEGF) Refined to 1.93 Å Resolution: Multiple Copy Flexibility and Receptor Binding. *Structure* **1997**, *5* (10), 1325–1338. https://doi.org/10.1016/S0969-2126(97)00284-0.

(33) Muller, Y. A.; Li, B.; Christinger, H. W.; Wells, J. A.; Cunningham, B. C.; de Vos, A. M. Vascular Endothelial Growth Factor: Crystal Structure and Functional Mapping of the Kinase Domain Receptor Binding Site. *Proc. Natl. Acad. Sci.* **1997**, *94* (14), 7192–7197. https://doi.org/10.1073/pnas.94.14.7192.

(34) Fuh, G.; Wu, P.; Liang, W.-C.; Ultsch, M.; Lee, C. V.; Moffat, B.; Wiesmann, C. Structure-Function Studies of Two Synthetic Anti-Vascular Endothelial Growth Factor Fabs and Comparison with the Avastin™ Fab. *J. Biol. Chem.* **2006**, *281* (10), 6625–6631. https://doi.org/10.1074/jbc.M507783200.

(35) Kim, K. J.; Li, B.; Winer, J.; Armanini, M.; Gillett, N.; Phillips, H. S.; Ferrara, N. Inhibition of Vascular Endothelial Growth Factor-Induced Angiogenesis Suppresses Tumour Growth in Vivo. *Nature* **1993**, *362* (6423), 841–844. https://doi.org/10.1038/362841a0.

(36) Lee, C. V.; Liang, W.-C.; Dennis, M. S.; Eigenbrot, C.; Sidhu, S. S.; Fuh, G. High-Affinity Human Antibodies from Phage-Displayed Synthetic Fab Libraries with a Single Framework Scaffold. *J. Mol. Biol.* **2004**, *340* (5), 1073–1093. https://doi.org/10.1016/j.jmb.2004.05.051.

(37) *DNA Structure and Function*; Elsevier, 1994. https://doi.org/10.1016/C2009-0-02451-9.

(38) Vo-Dinh, T.; Cullum, B. Biosensors and Biochips: Advances in Biological and Medical Diagnostics. *Fresenius J. Anal. Chem.* **2000**, *366* (6–7), 540–551. https://doi.org/10.1007/s002160051549.

(39) *Molecular Imprinting*; Haupt, K., Ayela, C., Eds.; Topics in current chemistry; Springer: Heidelberg ; New York, 2012.

(40) Singh, S.; Singh, P. K.; Umar, A.; Lohia, P.; Albargi, H.; Castañeda, L.; Dwivedi, D. K. 2D Nanomaterial-Based Surface Plasmon Resonance Sensors for Biosensing Applications. *Micromachines* **2020**, *11* (8), 779. https://doi.org/10.3390/mi11080779.

(41) Https://Phys.Libretexts.Org/Courses/Muhlenberg_College/Physics_122%3A_General_Physics_II_%28Collett%29/12%3A_The_Nature_of_Light/12.05%3A_Total_Internal_Reflection.

(42) Sato, Akihiro. Surface Plasmon Fluorescence Spectroscopy and Optical Waveguide Fluorescence Spectroscopy in Limit of Detection Studies, 2006.

(43) Gupta, B. D.; Verma, R. K. Surface Plasmon Resonance-Based Fiber Optic Sensors: Principle, Probe Designs, and Some Applications. *J. Sens.* **2009**, *2009*, 1–12. https://doi.org/10.1155/2009/979761.

(44) Darwish, I. A. Immunoassay Methods and Their Applications in Pharmaceutical Analysis: Basic Methodology and Recent Advances. *Int. J. Biomed. Sci. IJBS* **2006**, *2* (3), 217–235.

(45) Liu, L.; Gao, Y.; Liu, J.; Li, Y.; Yin, Z.; Zhang, Y.; Pi, F.; Sun, X. Sensitive Techniques for POCT Sensing on the Residues of Pesticides and Veterinary Drugs in Food. *Bull. Environ. Contam. Toxicol.* **2021**, *107* (2), 206–214. https://doi.org/10.1007/s00128-020-03035-0.

(46) Marx, K. A. Quartz Crystal Microbalance: A Useful Tool for Studying Thin Polymer Films and Complex Biomolecular Systems at the Solution−Surface Interface. *Biomacromolecules* **2003**, *4* (5), 1099–1120. https://doi.org/10.1021/bm020116i.

(47) Tetyana, P.; Morgan Shumbula, P.; Njengele-Tetyana, Z. Biosensors: Design, Development and Applications. In *Nanopores*; Ameen, S., Shaheer Akhtar, M., Shin, H.-S., Eds.; IntechOpen, 2021. https://doi.org/10.5772/intechopen.97576.

(48) Schmidt, K.; Hageneder, S.; Lechner, B.; Zbiral, B.; Fossati, S.; Ahmadi, Y.; Minunni, M.; Toca-Herrera, J. L.; Reimhult, E.; Barisic, I.; Dostalek, J. Rolling Circle Amplification Tailored for Plasmonic Biosensors: From Ensemble to Single-Molecule Detection. *ACS Appl. Mater. Interfaces* **2022**, *14* (49), 55017–55027. https://doi.org/10.1021/acsami.2c14500.